Parameterizing Eddy Buoyancy Fluxes Across Prograde Shelf/Slope Fronts Using a Slope-Aware GEOMETRIC Closure

HUAIYU WEI,[a,b] YAN WANG,[a,b] AND JULIAN MAK[a,b,c]

[a] Department of Ocean Science, The Hong Kong University of Science and Technology, Hong Kong, China
[b] Center for Ocean Research in Hong Kong and Macau, The Hong Kong University of Science and Technology, Hong Kong, China
[c] National Oceanography Centre, Southampton, United Kingdom

(Manuscript received 3 August 2023, in final form 6 October 2023, accepted 22 November 2023)

ABSTRACT: Accurate parameterizations of eddy fluxes across prograde, buoyant shelf and slope currents are crucial to faithful predictions of the heat transfer and water mass transformations in high-latitude ocean environments in ocean climate models. In this work we evaluate several parameterization schemes of eddy buoyancy fluxes in predicting the mean state of prograde current systems using a set of coarse-resolution noneddying simulations, the solutions of which are compared against those of fine-resolution eddy-resolving simulations with nearly identical model configurations. It is found that coarse-resolution simulations employing the energetically constrained GEOMETRIC parameterization can accurately reconstruct the prograde mean flow state, provided that the suppression of eddy buoyancy diffusivity over the continental slope is accounted for. The prognostic subgrid-scale eddy energy budget in the GEOMETRIC parameterization scheme effectively captures the varying trend of the domain-wide eddy energy level in response to environmental changes, even though the energy budget is not specifically designed for a sloping-bottomed ocean. Local errors of the predicted eddy energy are present but do not compromise the predictive skill of the GEOMETRIC parameterization for prograde current systems. This work lays a foundation for improving the representation of prograde current systems in coarse-resolution ocean climate models.

SIGNIFICANCE STATEMENT: The objective of this study is to evaluate different methods for predicting ocean volume transports caused by ocean mesoscale eddies across continental margins. This is important because these transports play a critical role in exchanges between coastal seas and open oceans, but cannot be resolved or well represented in ocean climate simulations. This study emphasizes the importance of accounting for the influence of sloping seafloors in controlling the eddy transport across the continental slope. This study also highlights the necessity of simultaneously predicting the eddy energy for better representation of the cross-slope eddy transport in ocean climate simulations.

KEYWORDS: Mesoscale processes; Eddies; General circulation models; Ocean models; Parameterization; Subgrid-scale processes

1. Introduction

Mesoscale eddies characterized by spatial scales of tens to hundreds of kilometers significantly modulate the ocean stratification and circulation by transporting and mixing oceanic properties (Danabasoglu et al. 1994; Lee et al. 2007), redistributing momentum (Greatbatch et al. 2010), and mediating energy transfer (Scott and Arbic 2007; Yankovsky et al. 2022). Despite their importance in ocean dynamics, mesoscale eddies cannot be fully resolved in current ocean climate models due to the limitation in computational power (Fox-Kemper et al. 2014, 2019). Consequently, mesoscale eddy processes are still commonly parameterized in ocean climate models.

The need for parameterizing mesoscale eddies is particularly pressing toward higher latitudes, where the eddy size decreases following the decline of the baroclinic Rossby deformation radius (Chelton et al. 1998; Hallberg 2013; LaCasce and Groeskamp 2020). In high-latitude regions, the planetary potential vorticity (PV) gradient diminishes and the environmental PV is increasingly dominated by the bottom topography. This is manifested by the local current systems steered heavily by the underlying sloping bathymetry, including the Antarctic Slope Current (ASC), the Norwegian Current, and the East and West Greenland Currents (Nøst and Isachsen 2003; Isachsen et al. 2003; Thompson and Heywood 2008; Trodahl and Isachsen 2018). These topographically steered currents can directly drive the oceanic meridional heat transports along the sloping bathymetry, forming surface branches of the global overturning circulation (Zhao et al. 2018). Moreover, these currents are observed to be baroclinically unstable (Isachsen 2015; Trodahl and Isachsen 2018), spawning mesoscale eddies that regulate mass and tracer fluxes across the sloping bottom (Hátún et al. 2007; Søiland and Rossby 2013). Prominent examples include eddies energized by the ASC, which modulate the ice shelf melting and bottom water transformation around Antarctica (Thompson et al. 2018; Stewart et al. 2018), and those produced in the northern subpolar/polar regions, which precondition the deep open ocean convection in the northern North Atlantic (Chanut et al. 2008; Spall 2010b) and govern the heat content in the ice-covered Arctic (Bashmachnikov et al. 2023).

One essential step toward faithful representations of the aforementioned mean current and eddy transports in predictive ocean climate models is in the accurate parameterization

---

Corresponding author: Yan Wang, yanwang@ust.hk

DOI: 10.1175/JPO-D-23-0152.1

of the eddy volume or buoyancy fluxes there. By incorporating the "correct" amount of eddy buoyancy fluxes, predictive ocean models are expected to represent these mean currents with reasonable frontal structures and thus baroclinic transports (via thermal wind balance; e.g., Mak et al. 2018; Kong and Jansen 2021) *along* the sloping bathymetry. In parallel, a "correct" parameterization of eddy buoyancy fluxes is necessary for reliable predictions of the mass and heat transfer *across* the sloping bathymetry, for instance, between the shallow shelf and deep open ocean (Si et al. 2023), thus capturing the impacts of boundary current systems on the interior ocean state.

In ocean climate models, mesoscale eddy buoyancy fluxes are routinely parameterized via the Gent–McWilliams (GM; Gent and McWilliams 1990) scheme, which formulates an eddy buoyancy diffusivity $\mathcal{K}_{\text{gm}}$ to inform the parameterized eddy buoyancy fluxes based on the model-resolved large-scale buoyancy gradients. The GM-based scheme incorporates the actions of mesoscale eddies to slump the large-scale isopycnals and thus to release the background available potential energy. One such broadly used representative GM-based scheme was developed by Visbeck et al. (1997), which tends to amplify the eddy buoyancy diffusivity across strong baroclinic ocean fronts. However, both theoretical and modeling studies show that eddy fluxes are effectively suppressed over sloping bathymetry (Blumsack and Gierasch 1972; Mechoso 1980; Spall 2004; Isachsen 2011; Brink 2012; Chen and Kamenkovich 2013; Brink and Cherian 2013; Stewart and Thompson 2013; Brink 2016; Cimoli et al. 2017; Hetland 2017; Manucharyan and Isachsen 2019; Chen et al. 2020; Si et al. 2022), contributing to the frontal current structures observed in high-latitude environments.

To address the above eddy parameterization issues, Wei et al. (2022) conducted a set of eddy-resolving simulations that account for two fundamental features of aforementioned topographically confined current systems: (i) a sloping ocean bottom that transitions from a shallow shelf region to the deep open ocean and (ii) a buoyant along-slope current with isopycnals tilted in the opposite direction to the ocean bottom. Such a current system has been conventionally termed "prograde" (e.g., Poulin et al. 2014). Wei et al. (2022) further proposed a diagnostic scaling for the cross-slope eddy buoyancy diffusivity. This scaling builds upon the GEOMETRIC parameterization of eddy buoyancy fluxes derived from quasigeostrophic (QG) turbulence models by Marshall et al. (2012); it establishes a linear relation between the total (potential plus kinetic) eddy energy and the eddy buoyancy diffusivity based on the mathematical bound of the geostrophic eddy stress tensor (Maddison and Marshall 2013; Bachman et al. 2017; Poulsen et al. 2019). To adapt the GEOMETRIC framework to prograde frontal systems and form a "slope-aware" scaling, Wei et al. (2022) integrated an analytical function of the slope Burger number (cf. section 3b) into the otherwise constant GEOMETRIC scaling prefactor (e.g., Mak et al. 2018), which enables the GEOMETRIC scaling to reproduce the diagnosed eddy buoyancy diffusivity across prograde fronts in the eddy-resolving simulations.

However, the diagnostic scaling of Wei et al. (2022) was not tested prognostically and thus carries uncertainties for use in coarse-resolution ocean models. In this follow-up work, we proceed to implement the slope-aware scaling of Wei et al. (2022) into a general circulation model and compare its skill with those of other GM-based schemes in predicting the mean state (e.g., baroclinic transport and stratification) of prograde current systems in coarse-resolution simulations. To this end, we invoke the closure of the subgrid-scale mesoscale eddy energy developed by Mak et al. (2018, 2022b), which has been primarily applied in open ocean environments. This readily leads to a more general assessment on the extent to which existing subgrid-scale eddy energy budgets (Mak et al. 2018, 2022b; Jansen et al. 2019; Kong and Jansen 2021) may facilitate the parameterizations of eddy fluxes across steep bottom slopes. Or, restated, we will concurrently probe the necessity of any substantial modification of available subgrid-scale eddy energy budgets (e.g., by refining the eddy energy advection, diffusion, or dissipation rate) for leveraging the prognostic efficacy of slope-aware forms of eddy buoyancy diffusivity in coarse-grid simulations with sloping bathymetry.

We find here that the slope-aware form of the GEOMETRIC scaling outperforms other GM-based schemes in predicting the prograde frontal structure in coarse-grid simulations, based on the "ground truth" solutions of the eddy-resolving runs of Wei et al. (2022). Moreover, our results indicate that, so long as the eddy buoyancy diffusivity is accurately formulated by taking the topographic effects into account, the mean state of prograde current systems in eddy-resolving runs can be adequately reconstructed by a coarse-grid model implemented with an otherwise unmodified, existing subgrid-scale eddy energy budget. The eddy energy budget, though suffering from local errors, correctly captures the bulk varying trend of parameterized eddy energy in response to the large-scale environmental changes (e.g., varied wind strengths).

The rest of this article is organized as follows. In section 2, we document the numerical experiments used in this study, outlining the similarities and distinctions between the coarse-resolution parameterized simulations and fine-resolution eddy-resolving simulations. In section 3, we review the GM-based eddy parameterization framework, introduce the selected GM-based parameterization schemes, and define the metrics used to assess the prognostic performance of selected schemes. In section 4, we quantify the relative merits of selected eddy parameterization schemes, among which the slope-aware form of the GEOMETRIC closure outperforms other GM-based schemes in predicting the prograde frontal structures in coarse-grid simulations. In section 5, we analyze the emergent eddy energy associated with the GEOMETRIC parameterization schemes, and explain how the predictive skill of the slope-aware GEOMETRIC closure is maintained in the presence of nontrivial local errors in the predicted eddy energy. Concluding remarks and discussions follow in section 6.

2. Model setup

This section outlines the configurations of numerical simulations used in this study. Two sets of simulations were conducted:

TABLE 1. List of parameters used in the reference fine-resolution simulation. The bold font denotes parameters that are independently varied among different model experiments.

	Value	Description
L_x	800 km	Zonal domain size
L_y	500 km	Meridional domain size
$H_{\max}$	4000 m	Maximum ocean depth
Δx	1 km	Horizontal grid spacing
Δz	10.5–103.8 m	Vertical grid spacing
H_s	3500 m	Shelf height
Z_s	2250 m	Slope middepth
Y_s	200 km	Midslope offshore position
W_s	50 km	**Slope half-width**
α_θ	1×10^{-4}°C^{-1}	**Thermal expansion coefficient**
τ_0	0.05 N m^{-2}	**Absolute wind stress maximum**
Y_w	200 km	Peak wind stress position
L_r	400 km	Meridional wind stress width
C_d	2.5×10^{-3}	Quadratic drag coefficient
A_4^m	0.1	Grid-dependent biharmonic viscosity
ρ_0	1000 kg m^{-3}	Reference Boussinesq density
g	9.81 m s^{-2}	Gravitational acceleration constant
f_0	1×10^{-4} s^{-1}	Constant Coriolis frequency

1) fine-resolution simulations, whose solutions serve as the ground truth, and 2) coarse-resolution simulations used to evaluate the prognostic performance of eddy parameterizations.

a. *Fine-resolution simulations*

The fine-resolution simulations used in this study are inherited from Wei et al. (2022) to quantify eddy-driven buoyancy fluxes across prograde shelf/slope fronts. The values of physical parameters adopted in the reference experiment are summarized in Table 1. This section briefly overviews the key model configurations used in Wei et al. (2022), to which the reader is referred for full model details.

All simulations are conducted via the MIT general circulation model (MITgcm hereafter; Marshall et al. 1997), which solves the hydrostatic, Boussinesq momentum equations. A linearized equation of state that only depends on potential temperature is adopted. The model domain is a reentrant channel on an *f* plane (with the Coriolis frequency $f_0 = 10^{-4}$ s^{-1}) that spans 800 km in the zonal (i.e., along-slope) direction and 500 km in the meridional (i.e., cross-slope) direction. The northern and southern boundaries are vertical walls imposed with no-normal-flow boundary conditions. The ocean depth increases offshore across an idealized continental slope and reaches its maximum of 4000 m at the northern boundary (Fig. 1a). Notice that the orientation of the continental slope relative to the meridians is dynamically irrelevant for rotationally invariant *f*-plane simulations.

The model is forced by a steady prograde (i.e., eastward or downwelling-favorable) wind stress peaked at the midslope location ($y = Y_s = 200$ km), where the seafloor is steepest. A quadratic drag is imposed at the ocean bed to extract momentum and energy. The potential temperature θ at the sea surface is restored to a profile that decays linearly northward, which sustains the horizontal stratification across the continental shelf and slope under the prograde wind forcing. At the northern boundary, a sponge layer of 50-km width is adopted to restore the potential temperature toward a reference exponential profile, which effectively fixes the first baroclinic Rossby deformation radius

$$L_d = \frac{1}{\pi f_0} \int_{-|H|}^{0} N dz \qquad (1)$$

at ~18 km at the northern boundary in the reference model run (H and N denote the ocean depth and buoyancy frequency, respectively). While L_d defined by Eq. (1) is an approximation to the standard deformation radius associated with the eigenvalue of the linearized QG PV equation under the Wentzel–Kramers–Brillouin approximation (Chelton et al. 1998), it is verified to be quantitatively accurate in our simulations (not shown).

Perturbation experiments were conducted to cover a broad range of prograde shelf/slope front configurations. In each of these

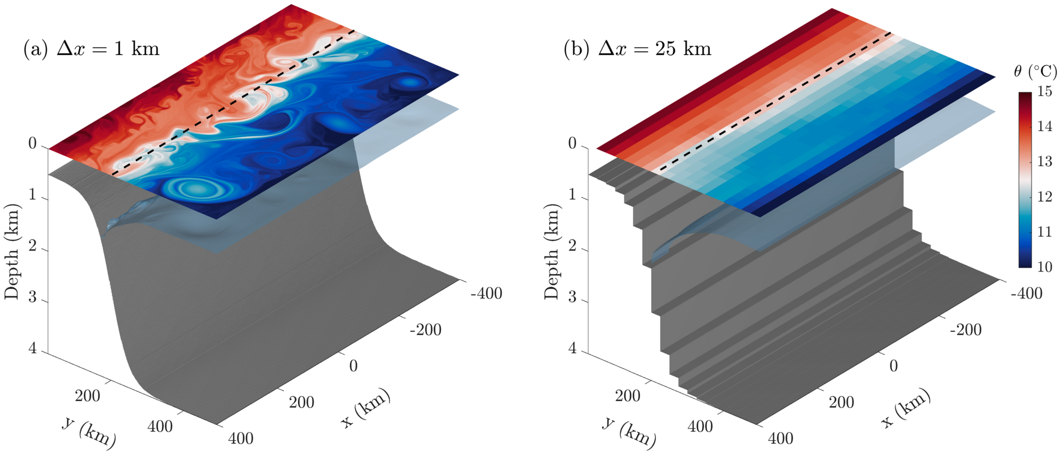

FIG. 1. Model bathymetry adopted in the (a) reference fine-resolution (1-km) simulation and (b) reference coarse-resolution (25-km) simulation with no GM-based parameterization enabled, superimposed by the instantaneous sea surface potential temperature (color shading) and the $\theta = 5$°C isotherm (semitransparent blue sheet). In both panels, the midslope position $y = Y_s = 200$ km is highlighted by the black dashed line.

TABLE 2. List of parameters varied among the perturbation experiments. The bold font highlights parameter values deviated from their reference values. The reader is referred to Table 1 for parameter definitions.

Experiment	W_s (km)	τ_0 (N m^{-2})	α_θ (10^{-4}°C^{-1})
$0.5W_s$	**25**	0.05	1.0
$0.66W_s$	**33**	0.05	1.0
Ref.	50	0.05	1.0
$1.5W_s$	**75**	0.05	1.0
$1.5\tau_0$	50	**0.075**	1.0
$2.0\tau_0$	50	**0.10**	1.0
$0.5\alpha_\theta$	50	0.05	**0.5**
$2.0\alpha_\theta$	50	0.05	**2.0**

experiments, one physical parameter (i.e., slope half-width W_s, peaking wind strength τ_0, or thermal expansion coefficient α_θ) is independently varied relative to the reference model run. Table 2 summarizes the perturbation experiments used in this study.

A sufficiently fine resolution (1 km in the horizontal and 70 vertical levels) was adopted to explicitly resolve the mesoscale processes over the continental shelf and slope ($L_d \simeq 10$ km at the midslope position upon flow equilibrium in the reference experiment). All simulations were integrated for at least 30 model years to achieve a statistically steady state, as revealed by the time series of domain-integrated total kinetic energy. Results presented in this work are calculated using model outputs time-averaged over the final 5 model years.

Figure 1a shows a snapshot of potential temperature at the sea surface (color shading) and the $\theta = 5$°C isotherm (semitransparent blue sheet) in the reference model run upon flow equilibrium. Mesoscale eddies are visible across the entire model domain. The selected isotherm (i.e., isopycnal) is tilted in the opposite direction of the topographic slope (with buoyant water piled shoreward), corresponding to a prograde current system (Isachsen et al. 2003; Nøst and Isachsen 2003; Spall 2010a; Pennel et al. 2012; Poulin et al. 2014; Isachsen 2015; Ghaffari et al. 2018).

b. Coarse-resolution simulations

To evaluate eddy parameterizations across prograde shelf/slope frontal systems, we further conducted coarse-resolution simulations incorporating various GM-based parameterizations (cf. section 3) by setting the horizontal grid spacing to 25 km. This grid spacing exceeds the first baroclinic deformation radius in the deep open ocean in all fine-resolution simulations upon flow equilibria. To ensure that the northern sponge layer consists of more than one grid point, both the channel width and the northern sponge layer are expanded 100 km northward in the coarse-resolution simulation. Other model configurations (e.g., bathymetry, external forcing, vertical resolution, and advection schemes) of the coarse-resolution runs exactly follow those of the fine-resolution simulations. Our selected GM-based schemes (cf. section 3b) are incorporated in these coarse-resolution simulations, and no parameterization of isopycnal diffusion (e.g., Redi 1982) is adopted. The coarse-resolution simulations were run from a resting state for 120 years to reach a statistically steady state, which is judged also from the time series of domain-integrated total kinetic energy. The time-averaged diagnostics were collected in the final 20 model years.

Figure 1b shows a snapshot of the sea surface potential temperature in the 25-km reference simulation with no GM-based parameterization enabled. Temperature deviations from the zonal-mean nearly vanish, suggesting that the 25-km horizontal grid spacing is not adequate to explicitly resolve mesoscale eddies in our model domain.

3. Theoretical background and parameterizations

a. Eddy buoyancy fluxes and the GM parameterization

When incorporating the GM-based parameterizations in coarse-resolution simulations, we opt for the skew flux formulation of eddy fluxes (Griffies 1998),

$$\begin{bmatrix} \mathcal{F}_b^x \\ \mathcal{F}_b^y \\ \mathcal{F}_b^z \end{bmatrix} = -\begin{bmatrix} 0 & 0 & -S^x\mathcal{K}_{\mathrm{gm}} \\ 0 & 0 & -S^y\mathcal{K}_{\mathrm{gm}} \\ S^x\mathcal{K}_{\mathrm{gm}} & S^y\mathcal{K}_{\mathrm{gm}} & 0 \end{bmatrix}\begin{bmatrix} \partial_x b \\ \partial_y b \\ \partial_z b \end{bmatrix}. \qquad (2)$$

Here $(\mathcal{F}_b^x, \mathcal{F}_b^y, \mathcal{F}_b^z)$ are the parameterized zonal, meridional, and vertical eddy buoyancy fluxes, (S^x, S^y) are the zonal and meridional isopycnal slopes resolved by coarse-resolution simulations, and $b = g\alpha_\theta\theta$ indicates the buoyancy with g denoting the gravitational acceleration constant. We have neglected the isopycnal diffusivity (e.g., Redi 1982) in Eq. (2), which makes no contribution to the simulated flow in our simulations because a linear equation of state with a single thermodynamic variable is adopted. Note further that the along-slope buoyancy flux $\mathcal{F}_b^x$ is included in Eq. (2) for completeness, but it does not influence the zonally averaged stratification in the reentrant channel considered in this work [i.e., the zonal average of $\partial_x(\mathcal{F}_b^x)$ is identically zero].

The parameterized eddy buoyancy flux following Eq. (2) is adiabatic[1] by construction because the flux direction is always parallel to that of the local isopycnal. For positive values of $\mathcal{K}_{\mathrm{gm}}$, the parameterized eddy fluxes reduce the horizontal buoyancy gradients and emulate the effect of eddies flattening the isopycnals. Notice that although $\mathcal{K}_{\mathrm{gm}}$ is commonly interpreted as the eddy buoyancy diffusivity, it is associated with the "skew flux" of buoyancy, as opposed to the diffusive flux (Griffies 1998; Abernathey et al. 2013; Kong and Jansen 2021).

According to Eq. (2), the eddy buoyancy diffusivity $\mathcal{K}_{\mathrm{gm}}$ must be specified for parameterizing the eddy buoyancy fluxes. Coarse-resolution ocean models differ substantially in their specifications of $\mathcal{K}_{\mathrm{gm}}$, which result in distinct parameterized eddy fluxes (e.g., Farneti et al. 2015). In this study, we evaluate the skills of various parameterization schemes in predicting the eddy buoyancy fluxes, as detailed in the next section.

---

[1] In practice, spurious diapycnal eddy flux components are present because of the spatial truncation errors associated with the advection operators acting on the parameterized eddy fluxes (Gerdes et al. 1991). In this study, we adopt the second-order-moment advection scheme of Prather (1986) to minimize this spurious mixing (Hill et al. 2012).

b. Selected GM-based parameterization schemes

We first consider a set of constant eddy buoyancy diffusivities

$$\mathcal{K}_{\mathrm{const}} \in [0, 50, 100, 150, 200, 250, 300]\,\mathrm{m^2\,s^{-1}}. \qquad (3)$$

The magnitudes of $\mathcal{K}_{\mathrm{const}}$ are chosen based on the cross-slope averaged eddy buoyancy diffusivity diagnosed from the fine-resolution simulations (cf. section 2a), most of which range from $\mathcal{O}(10^1)\,\mathrm{m^2\,s^{-1}}$ to $\mathcal{O}(10^2)\,\mathrm{m^2\,s^{-1}}$ (see Fig. 4d of Wei et al. 2022).

The second parameterization evaluated is the flow-dependent diffusivity proposed by Visbeck et al. (1997), i.e.,

$$\mathcal{K}_{\mathrm{visb}} = \alpha_{\mathrm{visb}} l_{\mathrm{visb}}^2 \langle \sigma_E \rangle, \qquad (4a)$$

$$\sigma_E = M^2/N. \qquad (4b)$$

Here $\alpha_{\mathrm{visb}} = 0.015$ represents a nondimensional constant prefactor derived by Visbeck et al. (1997) from a range of baroclinic processes, l_{visb} denotes the width of the baroclinic zone, which commonly serves as a tunable parameter (e.g., Kong and Jansen 2021), σ_E is the Eady (1949) growth rate, $M^2 = |\nabla_H b|$ measures the lateral stratification with ∇_H denoting the horizontal gradient operator, and $\langle \bullet \rangle = (1/|H|)\int_{-|H|}^{0} \bullet\, dz$ stands for the depth-average operator. As mentioned in section 1, the Visbeck et al. (1997) scheme tends to predict an enhanced eddy buoyancy diffusivity in frontal regions, where M^2 is large. The Visbeck et al. (1997) scheme (or parametrically similar variants) has been routinely implemented and used in predictive ocean simulations (Griffies et al. 2005; Farneti et al. 2010; Farneti and Gent 2011; Dunne et al. 2012; Todd et al. 2020; Uchida et al. 2020; Holmes et al. 2022).

A more elaborate eddy parameterization tested in this study is the energetically constrained GEOMETRIC framework (Marshall et al. 2012; Maddison and Marshall 2013). Under this framework, the eddy buoyancy diffusivity is formulated as (e.g., Mak et al. 2018, 2022a,b)

$$\mathcal{K}_{\mathrm{GEOM}} = \alpha_{\mathrm{geom}} \frac{\hat{E}}{\displaystyle\int_{-|H|}^{0} \sigma_E\, dz}, \qquad (5)$$

where $\alpha_{\mathrm{geom}} = \alpha_0$ denotes a nondimensional constant prefactor whose magnitude is bounded by unity in the QG limit, and $\hat{E} = \int_{-|H|}^{0} E\, dz$ stands for the depth-integrated total eddy energy per unit mass.

Last, we consider the modified version of the GEOMETRIC parameterization proposed by Wei et al. (2022) for prograde shelf/slope fronts, which accounts for the suppression of eddy diffusivity by the sloping ocean bed, i.e.,

$$\mathcal{K}_{\mathrm{GEOM}}^{\mathrm{slope}} = \alpha_{\mathrm{geom}} \frac{\hat{E}}{\displaystyle\int_{-|H|}^{0} \sigma_E\, dz}, \qquad (6a)$$

$$\alpha_{\mathrm{geom}} = \alpha_0 \mathcal{F}_{\mathrm{GEOM}} = \alpha_0 \frac{1}{\mu_1 \mathcal{S}^{\mu_2} + 1}, \qquad (6b)$$

where $\mu_1 = 7.8$ and $\mu_2 = 1.5$ are two constants derived empirically by Wei et al. (2022) from their high-resolution model diagnostics, and

$$\mathcal{S} = L_d \left| \frac{\nabla_H H}{H} \right| \qquad (7)$$

represents the slope Burger number (e.g., Brink 2016; Hetland 2017), whose variation is dominated by the seafloor steepness $|\nabla_H H|$ in our continental slope simulations. In this work, $|\nabla_H H|$ is calculated using central differencing based on adjacent water depths in the cross-slope direction. Note that the slope Burger number defined by Eq. (7) is more numerically compatible than that adopted in Wei et al. (2022), as it permits the direct use of any existing code that calculates the deformation radius in ocean general circulation models.

The scaling $\mathcal{K}_{\mathrm{GEOM}}^{\mathrm{slope}}$ defined by Eq. (6) is termed "slope-aware" and differs from $\mathcal{K}_{\mathrm{GEOM}}$ only by the inclusion of the $\mathcal{S}$-dependent function $\mathcal{F}_{\mathrm{GEOM}}$ in the nondimensional GEOMETRIC prefactor, which suggests a suppressed eddy buoyancy transport efficiency over a sloping ocean bed (i.e., $\mathcal{F}_{\mathrm{GEOM}} < 1$ for $\mathcal{S} > 0$). For a flat-bottomed ocean (i.e., $\mathcal{S} = 0$), $\mathcal{F}_{\mathrm{GEOM}}$ is identically unity, and $\mathcal{K}_{\mathrm{GEOM}}^{\mathrm{slope}}$ becomes equivalent to $\mathcal{K}_{\mathrm{GEOM}}$. Here we note that the magnitude of the GEOMETRIC prefactor defined in Marshall et al. (2012) depends on several eddy-related quantities [e.g., see γ_b in their Eq. (16)] and thus expected to be spatially variable [see also the diagnosed GEOMETRIC prefactor by Poulsen et al. (2019) from an eddy-permitting ocean model]. In the case of prograde slope fronts, Wei et al. (2022) have related the functional dependence of α_{geom} on the slope Burger number to the eddy growth rate across sloping seafloor, consistent with previous modeling studies (Brink 2012; Hetland 2017).

The eddy buoyancy diffusivity predicted by all tested GM variants is capped at $10^5\ \mathrm{m^2\,s^{-1}}$ to ensure numerical stability in coarse-resolution simulations. In addition, the Cox (1987) slope clipping is adopted with a maximal effective isopycnal slope set to 10^{-1}.

c. Subgrid-scale eddy energy budget

The GEOMETRIC variants $\mathcal{K}_{\mathrm{GEOM}}$ and $\mathcal{K}_{\mathrm{GEOM}}^{\mathrm{slope}}$ depend on the knowledge of depth-integrated total eddy energy $\hat{E}$ in coarse-resolution simulations. Mak et al. (2018) implemented a prognostic subgrid-scale eddy energy budget in MITgcm, which allowed their coarse-resolution simulations adopting $\mathcal{K}_{\mathrm{GEOM}}$ to broadly reproduce the sensitivity of the circumpolar transport to the changing surface winds as in eddy-permitting simulations. In this study, we directly use the prognostic subgrid eddy energy budget by Mak et al. (2018), formulated as

$$\underbrace{\frac{\partial}{\partial t}\hat{E}}_{\text{tendency}} + \underbrace{\frac{\partial}{\partial y}(\langle v \rangle \hat{E})}_{\text{advection}} = \underbrace{\int_{-|H|}^{0} \mathcal{K}_{\mathrm{gm}} \frac{M^4}{N^2}\, dz}_{\text{source}} - \underbrace{\tau_E^{-1}\hat{E}}_{\text{dissipation}} + \underbrace{\eta_E \frac{\partial^2}{\partial y^2}\hat{E}}_{\text{diffusion}}, \qquad (8)$$

in a zonally symmetric system. Here v is the resolved cross-slope velocity, τ_E denotes a linear eddy energy dissipation time scale (alternatively, τ_E^{-1} represents an energy dissipation rate), and η_E indicates the eddy energy diffusivity. The prognostic energy budget (8) was constructed based on the understanding that the mesoscale eddy energy is primarily sourced from baroclinic instability (e.g., Eady 1949; Phillips 1954), and could be advected (e.g., Klocker and Marshall 2014), diffused (e.g., Grooms 2017), and dissipated (e.g., energy flux out of the mesoscale; Mak et al. 2022a). Our simulations reveal a relative insensitivity of the simulated flow to the chosen energy diffusivity η_E, which is thus fixed as 500 m^2 s^{-1} following Mak et al. (2022a,b, 2023). Notice that the only adaption of the energy budget (8) to our simulations of prograde slope flows is the choice of GEOMETRIC variant (i.e., $\mathcal{K}_{\rm gm} \sim \mathcal{K}_{\rm GEOM}$ or $\mathcal{K}_{\rm gm} \sim \mathcal{K}_{\rm GEOM}^{\rm slope}$). More analyses about the utility of the energy budget (8) across prograde fronts in our simulations are provided in section 5.

d. Choices of tunable parameters

For prognostic calculations, the width of baroclinic zone $l_{\rm visb}$ in the Visbeck et al. (1997) scheme [Eq. (4)] must be specified; for the GEOMETRIC scheme, both the constant prefactor α_0 in Eqs. (5) and (6) and the energy dissipation time scale τ_E in the GEOMETRIC eddy energy budget (8) must be prescribed. Following previous prognostic studies of GM-based parameterizations (Hallberg 2013; Mak et al. 2018; Jansen et al. 2019; Kong and Jansen 2021), we determine these parameters by matching the simulated mean flow baroclinicity in the coarse-resolution simulations to that in the fine-resolution simulation of the reference experiment (Table 1). Specifically, the mean flow baroclinicity is quantified by the domain-averaged baroclinic velocity,

$$U_{\rm bc} = \{\overline{u}_{\rm bc}\} = \{\overline{u} - \overline{u}|_{z=-|H|}\}, \qquad (9)$$

where u is the along-slope velocity, the overbar indicates a time- and zonal-mean operator, and curly braces stand for a volume-mean operator across the coarse-resolution model domain[2] outside the northern sponge layer (i.e., $y \in [0, 450]$ km). The baroclinic velocity $\overline{u}_{\rm bc}$ is anticipated to be positive in prograde fronts, but negative values may arise in our simulations where the prograde wind forcing vanishes (e.g., $y > 400$ km). The calculated $U_{\rm bc}$ following Eq. (9) reflects the net domain-wide alongshore baroclinic transport, although excluding negative-valued $\overline{u}_{\rm bc}$ yields nearly indistinguishable results (not shown).

Following the above criterion, the length scale $l_{\rm visb}$ in $\mathcal{K}_{\rm visb}$ is tuned to be 50 km, which lies in the range of values used by previous studies (Farneti et al. 2010; Farneti and Gent 2011; Kong and Jansen 2021). For determining the two tunable parameters in the slope-aware GEOMETRIC variant $\mathcal{K}_{\rm GEOM}^{\rm slope}$, we opt to tune the energy dissipation time scale τ_E while fixing the prefactor α_0 as 0.07, a value diagnosed from our fine-resolution simulation diagnostics [see Fig. 4c of Wei et al. (2022); for comparison, Mak et al. (2023) set $\alpha_0 = 0.06$ for an idealized simulation of the Southern Ocean]. Solely tuning τ_E results in a time scale of 80 days, adhering to that used in Mak et al. (2023) and consistent with values estimated for the Southern Ocean based on inference calculation using hindcast outputs from a nominally 1/12° global simulation [see Fig. 4 of Mak et al. (2022a)]. Fixing τ_E while tuning α_0 yielded a similar skill of $\mathcal{K}_{\rm GEOM}^{\rm slope}$ in predicting the mean prograde current state (not shown).

For the slope-independent GEOMETRIC variant $\mathcal{K}_{\rm GEOM}$, we first evaluate its predictive skill with the same set of α_0 and τ_E as in its slope-aware counterpart $\mathcal{K}_{\rm GEOM}^{\rm slope}$. Then, α_0 and τ_E are independently adjusted to 0.04 or 40 days, with the thus formulated GEOMETRIC diffusivities denoted by $\mathcal{K}_{\rm GEOM}^{\downarrow\alpha_0}$ and $\mathcal{K}_{\rm GEOM}^{\downarrow\tau_E}$, respectively, to match the domain-averaged baroclinic velocity $U_{\rm bc}$ produced by coarse- and fine-resolution simulations. In appendix A, we document the sensitivity of $U_{\rm bc}$ to changes in α_0 and τ_E in the reference coarse-resolution simulations incorporating $\mathcal{K}_{\rm GEOM}$ or $\mathcal{K}_{\rm GEOM}^{\rm slope}$ (Fig. A1).

e. Assessment metrics

The domain-averaged baroclinic velocity $U_{\rm bc}$, defined via Eq. (9), serves as the first metric to quantify the domain-wide restratification parameterized by different GM variants.

While $U_{\rm bc}$ provides information about the parameterized domain-wide restratification, it may conceal local errors of simulated flow baroclinicity (i.e., positive and negative local biases may cancel out after the domain-average). To quantify the local prediction-truth deviation of flow resulting from different GM-based parameterizations, we further compute the bulk relative error of the baroclinic velocity,

$$\mathcal{E}_{\overline{u}_{\rm bc}} = \frac{\{|\overline{u}_{\rm bc}^{\rm CR} - \overline{u}_{\rm bc}^{\rm FR}|\}}{\{\overline{u}_{\rm bc}^{\rm FR}\}}. \qquad (10)$$

Here, the superscript CR denotes the quantity in the coarse-resolution simulation ($\Delta x = 25$ km), and the superscript FR denotes the quantity in the fine-resolution simulation ($\Delta x = 1$ km) that is coarse-grained onto the 25-km grid. Notice that $\mathcal{E}_{\overline{u}_{\rm bc}}$ is not necessarily small even when the domain-averaged baroclinic velocity $U_{\rm bc}$ in the parameterized simulation matches that in the fine-resolution simulation.

Previous studies also identified the local errors of buoyancy (or isopycnal interface height in isopycnal models) as a useful metric in assessing the skill of GM-based parameterizations (Jansen et al. 2019; Kong and Jansen 2021). The bulk relative error of potential temperature (equivalent to buoyancy in this work),

$$\mathcal{E}_{\overline{\theta}} = \frac{\{|\overline{\theta}^{\rm CR} - \overline{\theta}^{\rm FR}|\}}{\{\overline{\theta}^{\rm FR}\}}, \qquad (11)$$

is therefore chosen as an additional metric in this study. Notice that although $\mathcal{E}_{\overline{u}_{\rm bc}}$ and $\mathcal{E}_{\overline{\theta}}$ both evaluate the local reconstruction of stratification in coarse-resolution simulation, they emphasize different aspects of the simulated flow (i.e., cross-slope buoyancy gradient/frontal structure versus the buoyancy itself).

4. Performance of eddy parameterizations

In this section, we examine the performance of different GM-based parameterizations in predicting the flow baroclinicity of prograde shelf/slope fronts in our simulations. We

---

[2] If the volume-mean operator is applied on quantities from the fine-resolution simulation, these quantities have been coarse-grained onto the coarse-resolution grid.

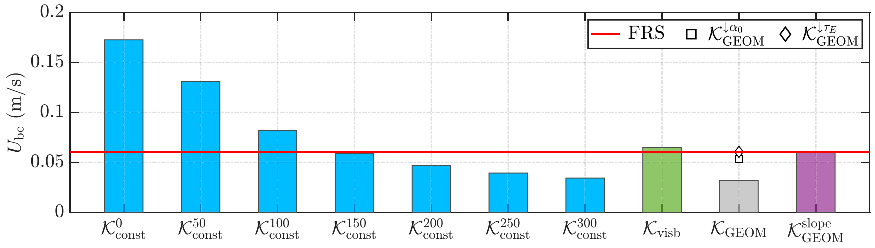

FIG. 2. The domain-averaged baroclinic velocity $U_{\rm bc}$ defined by Eq. (9) in the fine-resolution simulation (red line) and coarse-resolution simulations incorporating different GM-based parameterizations (bars and markers; see legend and labels on the abscissa).

first identify the "optimal" constant eddy diffusivity and verify the efficacy of selected flow-dependent GM variants in reconstructing the domain-wide flow baroclinicity in the reference experiment. Next, we compare the local flow baroclinicity produced by parameterized and eddy-resolving reference model runs. We then extend our analyses to a range of model configurations realized via the perturbation experiments (Table 2). Last, we provide insights into the distinct skills of different GM variants by discussing the prognostic eddy buoyancy diffusivities.

a. Parameterizing eddy fluxes in the reference experiment

1) SIMULATED DOMAIN-WIDE BAROCLINICITY IN THE REFERENCE EXPERIMENT

Figure 2 compares the domain-averaged baroclinic velocity $U_{\rm bc}$ in the fine-resolution simulation (red line) with those in coarse-resolution simulations that incorporate different GM-based parameterizations (bars and markers; superscripts of $\mathcal{K}_{\rm const}$ denote the specific values of the constant diffusivity). When the GM scheme is turned off in the coarse-resolution simulation (the simulation corresponding to $\mathcal{K}_{\rm const}^{0}$; see also Fig. 1b), $U_{\rm bc}$ is overestimated by a factor of ~3. The domain-averaged baroclinic velocity $U_{\rm bc}$ weakens as the magnitude of the constant diffusivity grows due to increasingly stronger restratification. The domain-averaged baroclinic velocity in the reference 1-km run ($U_{\rm bc} = 0.061$ m s^{-1}; red line) is most closely replicated by the 25-km simulation incorporating the constant eddy diffusivity of $\mathcal{K}_{\rm const}^{150}$ ($U_{\rm bc} = 0.059$ m s^{-1}). For a simulation incorporating $\mathcal{K}_{\rm visb}$, $\mathcal{K}_{\rm GEOM}^{\downarrow\alpha_0}$, $\mathcal{K}_{\rm GEOM}^{\downarrow\tau_E}$, or $\mathcal{K}_{\rm GEOM}^{\rm slope}$, $U_{\rm bc}$ also roughly matches that in the 1-km run, which is attributed to our optimal parameter tuning in the reference experiment. When the "untuned" GEOMETRIC variant $\mathcal{K}_{\rm GEOM}$ ($\alpha_0 = 0.07$, $\tau_E = 80$ days) is adopted, $U_{\rm bc}$ in the coarse-resolution simulation (0.032 m s^{-1}) is only half of that in the fine-resolution simulation, suggesting a domain-wide over-restratification.

2) SIMULATED LOCAL STRATIFICATION IN THE REFERENCE EXPERIMENT

In Fig. 3, we present the baroclinic velocity bias (color shadings)

$$\Delta\overline{u}_{\rm bc} = \overline{u}_{\rm bc}^{\rm CR} - \overline{u}_{\rm bc}^{\rm FR} \qquad (12)$$

as a function of depth and offshore distance produced by coarse-resolution simulations incorporating different GM-based parameterizations in the reference experiment. In prograde fronts, $\overline{u}_{\rm bc}$ is dominantly positive, and $\Delta\overline{u}_{\rm bc} > 0$ ($\Delta\overline{u}_{\rm bc} < 0$) therefore implies underpredicted (overpredicted) eddy restratification. Selected isotherms produced by the 1-km run (black curves) and 25-km runs (green curves) are further superposed to evaluate the local temperature reconstruction by the selected GM variants. Specifically, the temperature warm (cold) biases arise if the isotherms are deeper (shallower) in 25-km runs than those in the 1-km run.

Similar spatial patterns of $\Delta\overline{u}_{\rm bc}$ are found in coarse-resolution simulations incorporating $\mathcal{K}_{\rm const}^{150}$, $\mathcal{K}_{\rm visb}$, $\mathcal{K}_{\rm GEOM}^{\downarrow\alpha_0}$, and $\mathcal{K}_{\rm GEOM}^{\downarrow\tau_E}$ (Figs. 3a,b,d,e), with the local baroclinic velocity overestimated over the continental slope (i.e., $y \in [150, 250]$ km) and underestimated in relatively flat-bottomed regions (i.e., $y < 150$ km or $y > 250$ km). Since the temperature profile is effectively fixed by the northern sponge layer, the overestimated baroclinic velocity (and thus offshore buoyancy gradient) in the open ocean (red shadings) leads to warm temperature anomalies there, as manifested by the deeper isopycnals in coarse-resolution simulation (dashed curves) than those in fine-resolution simulation (solid curves). Toward the continental slope, warm temperature anomalies diminish and cold temperature anomalies arise, consistent with the underestimated $\overline{u}_{\rm bc}$ (blue shadings). It is worth noting that although the GM variants $\mathcal{K}_{\rm const}^{150}$, $\mathcal{K}_{\rm visb}$, $\mathcal{K}_{\rm GEOM}^{\downarrow\alpha_0}$, and $\mathcal{K}_{\rm GEOM}^{\downarrow\tau_E}$ can reasonably reconstruct the *domain-wide* baroclinic transport (Fig. 2), they lead to large *local* errors in the flow baroclinicity (e.g., $|\Delta\overline{u}_{\rm bc}|$ can exceed 0.50 m s^{-1}).

When the 25-km run adopts $\mathcal{K}_{\rm GEOM}$ (Fig. 3d), isopycnals in the open-ocean region ($y > 250$ km) nearly match those in the fine-resolution simulation, but the flow is overly stratified over the continental slope, with $\Delta\overline{u}_{\rm bc}$ reaching a minimum of -0.72 m s^{-1}. This overestimated eddy restratification in the slope region is expected, as $\mathcal{K}_{\rm GEOM}$ agrees primarily with eddy diffusivities diagnosed in the relatively flat-bottomed open ocean environments (Wang and Stewart 2020; Wei et al. 2022). By replacing the constant prefactor α_0 in $\mathcal{K}_{\rm GEOM}$ with $\alpha_0\mathcal{F}_{\rm GEOM}$ following Eq. (6b), the slope-aware GEOMETRIC parameterization $\mathcal{K}_{\rm GEOM}^{\rm slope}$ alleviates the prediction biases shown in other simulations (Fig. 3f), especially over the continental slope ($|\Delta\overline{u}_{\rm bc}|$ stays below 0.30 m s^{-1}). Consistently, the predicted isopycnals in the coarse-resolution simulation with $\mathcal{K}_{\rm GEOM}^{\rm slope}$ most accurately match those in the fine-resolution simulation. It is worth noting that the minimized $\Delta\overline{u}_{\rm bc}$ and the optimally matched isopycnals by the slope-aware GEOMETRIC variant $\mathcal{K}_{\rm GEOM}^{\rm slope}$ cannot be achieved by the slope-independent

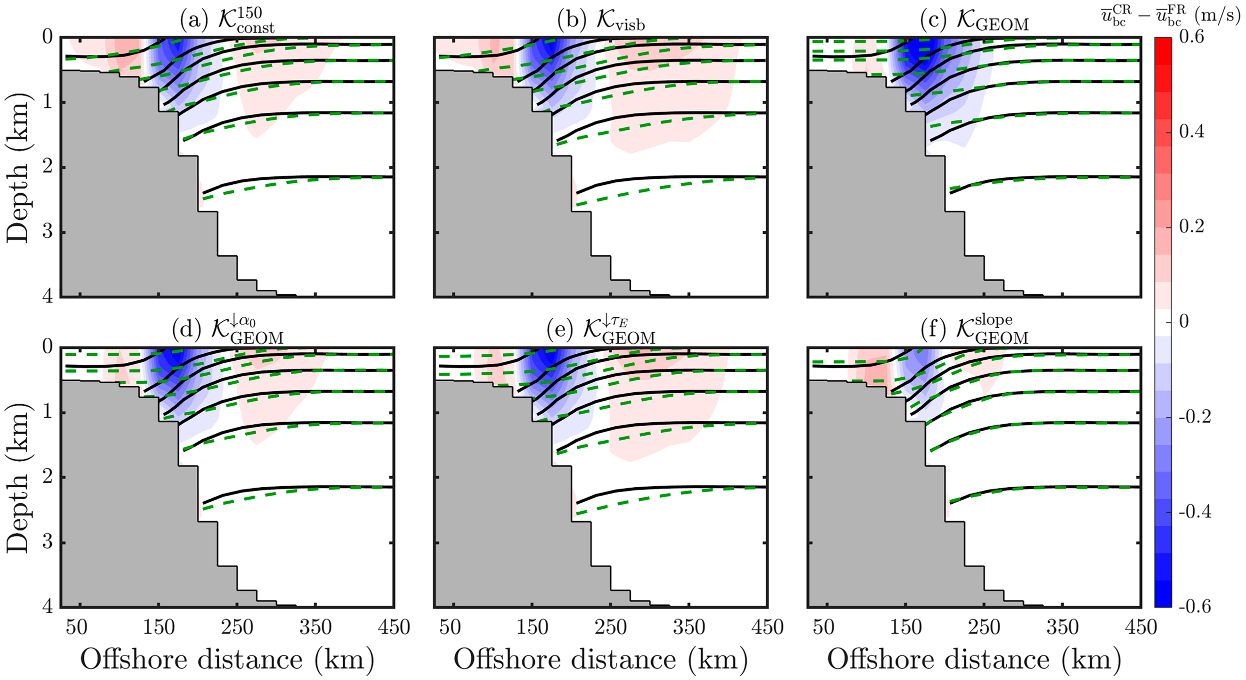

FIG. 3. Comparison of time- and zonal-mean baroclinic velocity and stratification between the fine-resolution simulation and coarse-resolution simulations incorporating (a) $\mathcal{K}^{150}_{\rm const}$, (b) $\mathcal{K}_{\rm visb}$, (c) $\mathcal{K}_{\rm GEOM}$, (d) $\mathcal{K}^{\downarrow\alpha_0}_{\rm GEOM}$, (e) $\mathcal{K}^{\downarrow\tau_E}_{\rm GEOM}$, and (f) $\mathcal{K}^{\rm slope}_{\rm GEOM}$ in the reference experiment. Red (blue) shading indicates overestimated (underestimated) baroclinic velocity in coarse-resolution simulations. Black solid (green dashed) contours indicate time- and zonal-mean isopycnals starting from 1°C with an interval of 2°C in the fine-resolution simulation (coarse-resolution simulations).

GEOMETRIC variant (i.e., $\alpha_{\rm geom} = \alpha_0$), no matter how the parameters α_0 and λ_E are adjusted (Figs. 3d,e).

To quantitatively measure the local biases of $\overline{u}_{\rm bc}$ and $\overline{\theta}$ observed in Fig. 3, we present in Fig. 4 the bulk relative errors $\mathcal{E}_{\overline{u}_{\rm bc}}$ and $\mathcal{E}_{\overline{\theta}}$ defined by Eqs. (10) and (11), respectively. The constant diffusivity $\mathcal{K}^{150}_{\rm const}$, which produces the best matched $U_{\rm bc}$, also minimizes relative errors in the coarse-resolution simulation among all constant diffusivities ($\mathcal{E}_{\overline{u}_{\rm bc}} = 61.1\%$ and $\mathcal{E}_{\overline{\theta}} = 5.7\%$). We therefore refrain from discussing constant eddy diffusivities other than $\mathcal{K}^{150}_{\rm const}$ in subsequent analyses.

Despite the parametric dependence of $\mathcal{K}_{\rm visb}$ and $\mathcal{K}_{\rm GEOM}$ on the mean flow, the resulting relative errors are even larger than those corresponding to the constant diffusivity $\mathcal{K}^{150}_{\rm const}$ (e.g., $\mathcal{E}_{\overline{u}_{\rm bc}} = 63.8\%$ and $\mathcal{E}_{\overline{\theta}} = 10.2\%$ for $\mathcal{K}_{\rm GEOM}$). Tuning $\alpha_{\rm geom}$ or τ_E in the GEOMETRIC scheme without adding the slope-aware modification does not qualitatively improve the reconstructed baroclinic velocity (e.g., $\mathcal{E}_{\overline{u}_{\rm bc}} = 62.6\%$ and $\mathcal{E}_{\overline{\theta}} = 7.7\%$ for $\mathcal{K}^{\downarrow\alpha_0}_{\rm GEOM}$). Last, the slope-aware GEOMETRIC variant $\mathcal{K}^{\rm slope}_{\rm GEOM}$ exhibits the best skill in predicting the local flow stratification among all tested GM variants in the reference coarse-resolution simulations, yielding $\mathcal{E}_{\overline{u}_{\rm bc}} = 33.5\%$ and $\mathcal{E}_{\overline{\theta}} = 2.8\%$.

b. *Parameterization performance in perturbation experiments*

The analyses in the reference calculation show that the slope-aware GEOMETRIC parameterization $\mathcal{K}^{\rm slope}_{\rm GEOM}$ [Eq. (6)] outperforms other tested GM-based schemes in reconstructing the mean flow state in coarse-resolution simulations. However, it remains unclear whether similar conclusions hold across a wide range of physical parameters. In this section, we utilize the perturbation experiments (Table 2) to assess the performance of selected GM-based parameterization schemes without any retuning (i.e., by setting the tunable parameters identical to those in the reference experiment). We start again by investigating how well the selected GM variants reconstruct the domain-averaged baroclinic velocity $U_{\rm bc}$ in all experiments. Then we analyze the relative errors $\mathcal{E}_{\overline{u}_{\rm bc}}$ and $\mathcal{E}_{\overline{\theta}}$ to assess the reconstruction of the local mean current state by different GM variants in all perturbation experiments.

1) SIMULATED DOMAIN-WIDE BAROCLINICITY IN PERTURBATION EXPERIMENTS

In Fig. 5, we compare the domain-averaged baroclinic velocity $U_{\rm bc}$ in fine-resolution simulations (red lines) against those produced by coarse-resolution simulations incorporating different GM variants (bars and markers) in all perturbation experiments. The "untuned" GEOMETRIC variant $\mathcal{K}_{\rm GEOM}$ (gray bars) produces consistently underestimated $U_{\rm bc}$ by overly restratifying the flow in all experiments. In experiments with varied slope half-width (i.e., $0.5W_s$, $0.66W_s$, and $1.5W_s$) or thermal expansion coefficient (i.e., $0.5\alpha_\theta$ and $2\alpha_\theta$), GM variants other than $\mathcal{K}_{\rm GEOM}$ exhibit qualitatively similar skills in predicting the bulk flow baroclinicity. Analyses of the parameterized eddy fluxes reveal that the analogously

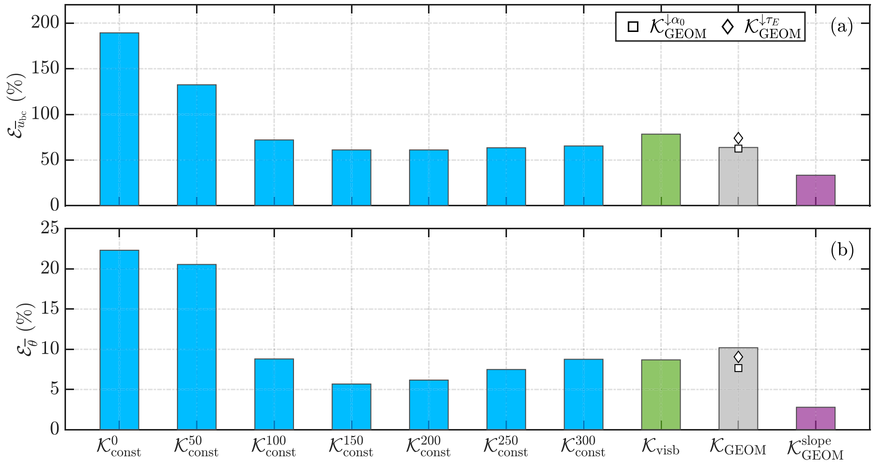

FIG. 4. Bulk relative errors of the mean (a) baroclinic velocity $\mathcal{E}_{\overline{u}_{bc}}$ and (b) potential temperature $\mathcal{E}_{\overline{\theta}}$ produced by coarse-resolution simulations incorporating different GM-based parameterizations (see legend and labels on the abscissa) in the reference experiment.

predicted U_{bc} by these GM variants in each perturbation experiment is related to the nearly identical domain-wide restratification (i.e., domain-averaged buoyancy fluxes $\{\mathcal{F}_b^y\}$) predicted by different GM variants, despite their distinct cross-slope variations. Specifically, the standard deviation of predicted $\{\mathcal{F}_b^y\}$ by GM variants other than $\mathcal{K}_{\mathrm{GEOM}}$ is less than 8% relative to their mean value in each perturbation experiment with varied α_θ or W_s (not shown).

Experiments with varied winds (i.e., $1.5\tau_0$ and $2\tau_0$) reveal better skills of energetically constrained GM variants in reconstructing the bulk flow baroclinicity. When $\mathcal{K}^{150}_{\mathrm{const}}$ and $\mathcal{K}_{\mathrm{visb}}$ are adopted (blue and green bars), the increment of U_{bc} with strengthened winds is overestimated. In specific, U_{bc} increases from 0.059 to 0.127 m s^{-1} (from 0.061 to 0.070 m s^{-1}) in the 25-km run adopting $\mathcal{K}^{150}_{\mathrm{const}}$ (1-km run) as the wind strength is doubled. When the coarse-resolution simulations incorporate $\mathcal{K}_{\mathrm{visb}}$, the overestimated increment of U_{bc} with strengthened winds is slightly alleviated (U_{bc} increases from 0.065 to 0.106 m s^{-1}) compared to the case of $\mathcal{K}^{150}_{\mathrm{const}}$. This alleviation is due to the enhanced eddy restratification predicted by $\mathcal{K}_{\mathrm{visb}}$ in the $2\tau_0$ experiment, as the isopycnals are steepened by wind. However, the restratification induced by the Visbeck et al. (1997) scheme is still too weak under stronger winds compared to the case of fine-resolution simulations. When the energetically constrained GEOMETRIC schemes, $\mathcal{K}^{\downarrow\alpha_0}_{\mathrm{GEOM}}$, $\mathcal{K}^{\downarrow\tau_E}_{\mathrm{GEOM}}$, or $\mathcal{K}^{\mathrm{slope}}_{\mathrm{GEOM}}$, serve as the GM-based eddy closure (markers and purple bars), the 25-km simulations effectively capture the growth of U_{bc} in response to strengthened winds, with the U_{bc} bias staying below 0.015 m s^{-1}. Note also that although the GEOMETRIC variant $\mathcal{K}_{\mathrm{GEOM}}$ produces consistently underestimated U_{bc}, it still correctly captures the increasing trend of U_{bc} with strengthened winds. The accurately predicted sensitivity of U_{bc} to varied winds by GEOMETRIC parameterizations is primarily attributed to the response of domain-averaged subgrid-scale eddy energy to surface winds, which will be discussed in more detail in section 5.

2) SIMULATED LOCAL STRATIFICATION IN PERTURBATION EXPERIMENTS

As discussed in section 4a, while U_{bc} provides a useful metric for the domain-wide parameterized eddy restratification, nonnegligible local errors of simulated flow baroclinicity may exist. We therefore assess the performance of different GM variants in reproducing the local $\overline{u}_{bc}$ and $\overline{\theta}$ in all coarse-

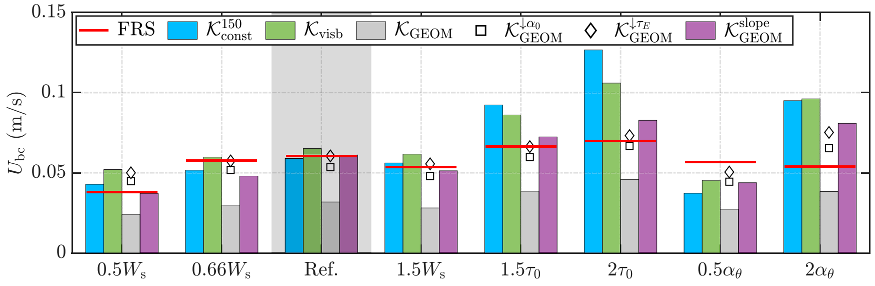

FIG. 5. The domain-averaged baroclinic velocity U_{bc} in the fine-resolution simulations (red lines) against those in the coarse-resolution simulations incorporating different GM variants (bars and markers; see legend) in all perturbation experiments (see labels on the abscissa and Table 2). The gray shading highlights the reference experiment.

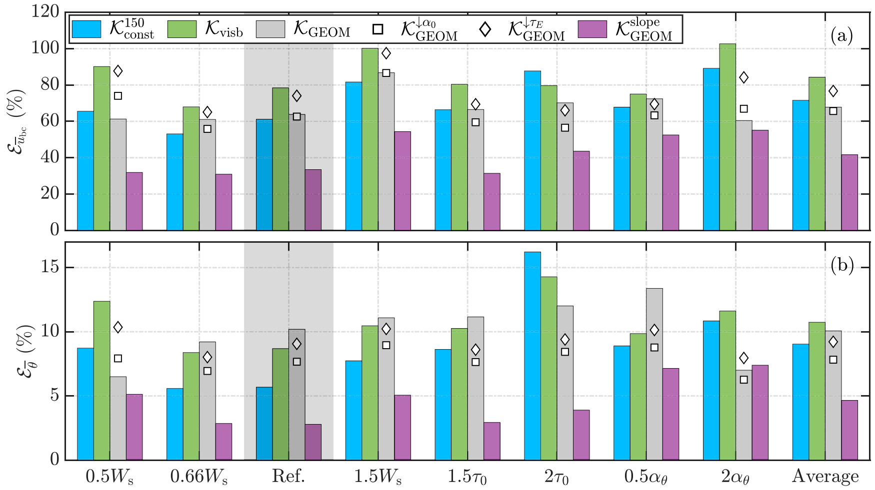

FIG. 6. Bulk relative errors of the mean (a) baroclinic velocity $\mathcal{E}_{\overline{u}_{\rm bc}}$ and (b) potential temperature $\mathcal{E}_{\overline{\theta}}$ produced by coarse-resolution simulations incorporating different GM-based parameterizations (bars and markers; see legend) in all perturbation experiments (see labels on the abscissa and Table 2). The relative errors averaged across all experiments are shown via the rightmost column in each panel. In both panels, the gray shading highlights the reference experiment.

resolution experiments (Fig. 6). When the coarse-resolution simulations incorporate the constant diffusivity $\mathcal{K}_{\rm const}^{150}$ (blue bars), $\mathcal{E}_{\overline{u}_{\rm bc}}$ and $\mathcal{E}_{\overline{\theta}}$ averaged across all experiments (see the rightmost panel) are 71.5% and 9.0%, respectively. The overall performance of the Visbeck et al. (1997) scheme (green bars) is slightly worse than the constant diffusivity $\mathcal{K}_{\rm const}^{150}$ in local stratification reconstruction ($\mathcal{E}_{\overline{u}_{\rm bc}} = 84.3\%$ and $\mathcal{E}_{\overline{\theta}} = 10.7\%$ averaged across all experiments), though $\mathcal{K}_{\rm const}^{150}$ yields the largest $\mathcal{E}_{\overline{\theta}}$ in the $2\tau_0$ experiment. The slope-independent GEOMETRIC variants (gray bars and markers) show similar skills in reconstructing the local baroclinicity as $\mathcal{K}_{\rm const}^{150}$ and $\mathcal{K}_{\rm visb}$ ($\mathcal{E}_{\overline{u}_{\rm bc}} = 67.8\%$, 65.7%, and 76.7% averaged across all experiments for $\mathcal{K}_{\rm GEOM}$, $\mathcal{K}_{\rm GEOM}^{\downarrow\alpha_0}$, and $\mathcal{K}_{\rm GEOM}^{\downarrow\tau_{\rm E}}$, respectively). Consistent with the results in the reference experiment (Fig. 4), the slope-aware GEOMETRIC variant $\mathcal{K}_{\rm GEOM}^{\rm slope}$ (purple bars) most accurately predicts the baroclinic velocity and buoyancy fields in all other perturbation experiments, with $\mathcal{E}_{\overline{u}_{\rm bc}}$ and $\mathcal{E}_{\overline{\theta}}$ averaged across all experiments being as low as 41.7% and 4.7%, respectively.

Given the efficacy of the slope-dependent function $\mathcal{F}_{\rm GEOM}$ in adapting the GEOMETRIC scheme to prograde slope flows, one may wonder whether similar modifications can be made to the Visbeck et al. (1997) scheme or even an otherwise constant diffusivity such that the prediction biases associated with these GM-based closures can be mitigated. We have conducted additional coarse-resolution simulations incorporating two modified GM-based schemes, $\mathcal{F}_{\rm GEOM}\mathcal{K}_{\rm const}$ and $\mathcal{F}_{\rm GEOM}\mathcal{K}_{\rm visb}$, in all perturbation experiments. For these modified schemes, we set $\mathcal{K}_{\rm const} = 300\,{\rm m^2\,s^{-1}}$ and $l_{\rm visb} = 80$ km to attain matched $U_{\rm bc}$ produced by coarse- and fine-resolution simulations in the reference experiment (cf. section 3d). Adding the slope-dependent function indeed alleviates the prediction biases in both cases [$\mathcal{E}_{\overline{\theta}} = 7.3\%$ and 8.2% averaged across all experiments for the modified "constant" diffusivity and Visbeck et al. (1997) scheme, respectively; not shown]. Nevertheless, the slope-aware GEOMETRIC variant still yields the most accurate prediction of the local stratification among all closures considered across our coarse-resolution simulations.

In summary, the energetically constrained GEOMETRIC variants exhibit a better skill in capturing the sensitivity of domain-wide baroclinic transport to varied winds, and the slope-aware form of the GEOMETRIC closure $\mathcal{K}_{\rm GEOM}^{\rm slope}$ outperforms other GM-based schemes in reconstructing the local density structure of prograde fronts in coarse-resolution simulations across a wide range of physical parameters. The superior performance of $\mathcal{K}_{\rm GEOM}^{\rm slope}$ cannot be achieved by solely tuning $\alpha_{\rm geom}$ or τ_E in $\mathcal{K}_{\rm GEOM}$, which highlights the necessity to incorporate the topographic suppression effects of eddy buoyancy fluxes across the sloping seafloor.

c. *Prognostic eddy buoyancy diffusivities*

To further interpret the local mismatch between coarse- and fine-resolution simulations, we plot in Fig. 7 the prognostic diffusivities (colored curves) predicted by different GM-based parameterizations upon flow equilibria in coarse-resolution simulations as functions of offshore distance in the reference experiment, along with the diagnosed depth-averaged eddy buoyancy diffusivity (black dots),

$$\mathcal{K}_{\rm diag} = \langle \overline{v'b'} \rangle / \langle \partial_y \overline{b} \rangle, \tag{13}$$

in the reference fine-resolution simulation. Here, the prime ($\bullet' = \bullet - \overline{\bullet}$) stands for the deviation from the time and zonal mean.

The constant diffusivity $\mathcal{K}_{\rm const}^{150}$ (blue line) is overall weaker (stronger) than $\mathcal{K}_{\rm diag}$ in the open ocean (over the continental slope), and therefore results in an underestimated (overestimated) eddy restratification in the 25-km run compared

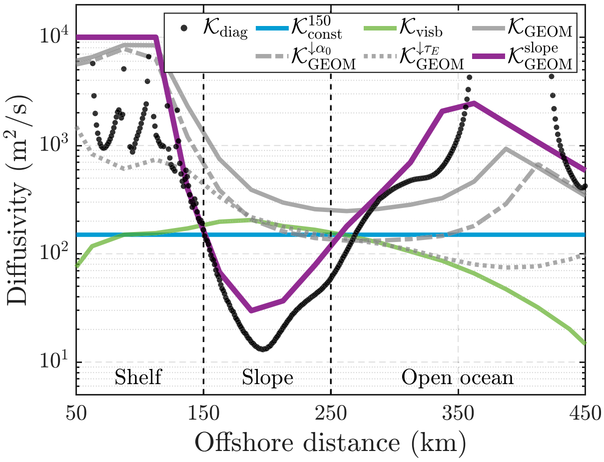

FIG. 7. Eddy buoyancy diffusivity diagnosed in the fine-resolution simulation (black dots) and produced by different GM-based parameterizations in the coarse-resolution simulations (curves; see legend) as functions of offshore distance in the reference experiment upon dynamic equilibria.

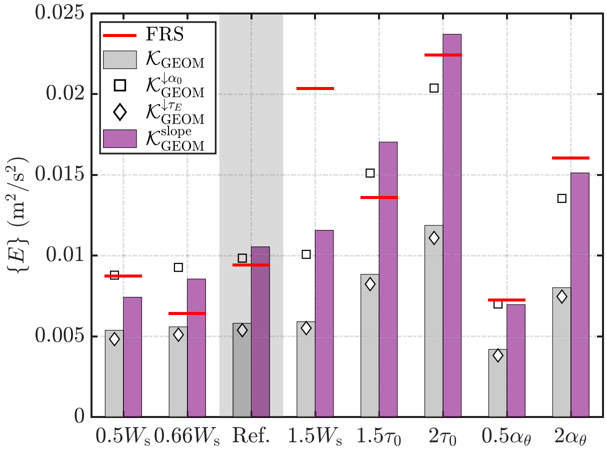

FIG. 8. The domain-averaged total eddy energy $\{E\}$ diagnosed in fine-resolution simulations (red lines) against those in coarse-resolution simulations incorporating $\mathcal{K}_{\mathrm{GEOM}}$ (gray bars), $\mathcal{K}_{\mathrm{GEOM}}^{\downarrow\alpha_0}$ (squares), $\mathcal{K}_{\mathrm{GEOM}}^{\downarrow\tau_E}$ (diamonds), and $\mathcal{K}_{\mathrm{GEOM}}^{\mathrm{slope}}$ (purple bars) in all perturbation experiments (see labels on the abscissa and Table 2).

against the 1-km run, consistent with positive (negative) values of $\Delta\overline{u}_{\mathrm{bc}}$ and steeper (flatter) isopycnals as shown in Fig. 3b.

The diffusivity predicted by the Visbeck et al. (1997) scheme (green curve) shows a similar magnitude as $\mathcal{K}_{\mathrm{const}}^{150}$ to the south of $y = 350$ km, and its spatial variation exactly opposes the profile of the true eddy diffusivity $\mathcal{K}_{\mathrm{diag}}$. Specifically, while $\mathcal{K}_{\mathrm{visb}}$ peaks at 205 m^2 s^{-1} over the continental slope ($y = 188$ km), the diagnosed diffusivity $\mathcal{K}_{\mathrm{diag}}$ reaches a global minimum of 13 m^2 s^{-1} at $y = 197$ km. The magnitude of $\mathcal{K}_{\mathrm{visb}}$ is proportional to the Eady (1949) growth rate $\langle\sigma_E\rangle$ (this growth rate is dominated by M^2 in our simulations) following Eq. (4) and is therefore enhanced across the frontal zone over the continental slope. The opposite profile of $\mathcal{K}_{\mathrm{visb}}$ to that of $\mathcal{K}_{\mathrm{diag}}$ explains the overall worse performance of the Visbeck et al. (1997) scheme than the constant diffusivity $\mathcal{K}_{\mathrm{const}}^{150}$ in reconstructing the local stratification, as indicated by the bulk relative errors in Fig. 4. These results are consistent with the assertion of Isachsen (2011) that a GM-based closure proportional to the thermal wind velocity may effectively "wash out" the frontal structures of topographically steered ocean currents.

When the untuned GEOMETRIC parameterization $\mathcal{K}_{\mathrm{GEOM}}$ is adopted (solid gray curve in Fig. 7), no obvious eddy suppression is detected across the sloping bottom. Consequently, $\mathcal{K}_{\mathrm{GEOM}}$ significantly exceeds $\mathcal{K}_{\mathrm{diag}}$ over the continental slope (e.g., $\mathcal{K}_{\mathrm{GEOM}} = 390\,\mathrm{m}^2\,\mathrm{s}^{-1}$ versus $\mathcal{K}_{\mathrm{diag}} = 15\,\mathrm{m}^2\,\mathrm{s}^{-1}$ at $y = 188$ km), yielding overly flattened isopycnals there (Fig. 3c). With reduced α_{geom} or τ_E, the predicted diffusivity $\mathcal{K}_{\mathrm{GEOM}}^{\downarrow\alpha_0}$ and $\mathcal{K}_{\mathrm{GEOM}}^{\downarrow\tau_E}$ (dashed and dotted curves) decreases in magnitude across both the continental slope and open ocean regions compared to the prediction by $\mathcal{K}_{\mathrm{GEOM}}$. Notably, the order-of-magnitude decrease of $\mathcal{K}_{\mathrm{diag}}$ from the open ocean toward continental slope cannot be captured by simply retuning the value of α_{geom} or τ_E. On the contrary, the prognostic diffusivity predicted by the slope-aware GEOMETRIC parameterization (purple curve) quantitatively captures the variation of $\mathcal{K}_{\mathrm{diag}}$ (e.g., both $\mathcal{K}_{\mathrm{GEOM}}^{\mathrm{slope}}$ and $\mathcal{K}_{\mathrm{diag}}$ decrease by two orders of magnitude from $y = 363$ km to $y = 188$ km), consistent with the minimal $\overline{u}_{\mathrm{bc}}$ and $\overline{\theta}$ errors shown in Figs. 3f and 4.

In appendix B, we present the prognostic eddy buoyancy diffusivity predicted by the selected GM variants along with the diagnosed diffusivity in all perturbation experiments (Fig. B1). The aforementioned characteristics of the prognostic and diagnosed eddy diffusivity in the reference simulation apply to all other experiments.

5. Emergent eddy energy

It is noteworthy that the energetically constrained slope-aware GEOMETRIC parameterization has shown a promising skill in reproducing the flow baroclinicity (both in bulk and local senses) across prograde fronts, despite the fact that the subgrid-scale eddy energy budget is not specifically designed for a sloping-bottomed ocean. In this section, we examine the extent to which the prognostic eddy energy budget (8) in coarse-resolution simulations can quantify the true eddy energy in fine-resolution simulations. Investigating the prognostic eddy energy also helps to elucidate the relative importance of the specific parameter dependence and the parameterized eddy energy to the predictive skill of the GEOMETRIC parameterization.

a. Domain-wide eddy energy

In Fig. 8, we show the domain-averaged prognostic eddy energy $\{E\}$ in 25-km simulations incorporating GEOMETRIC variants (bars and markers), along with the diagnosed $\{E\}$ in 1-km runs (red lines; see appendix C for the detailed formulation) across all perturbation experiments. The diagnosed total eddy energy in fine-resolution simulations is reasonably captured by the prognostic eddy energy budget with $\mathcal{K}^{\text{slope}}_{\text{GEOM}}$ (purple bars) and $\mathcal{K}^{\downarrow\alpha_0}_{\text{GEOM}}$ (squares) in all experiments except for the case with the gentlest sloping bottom (i.e., $1.5W_s$). The consistency between the diagnosed and predicted $\{E\}$ is particularly obvious in simulations with varied winds or thermal expansion coefficients. The similar magnitudes of $\{E\}$ in simulations with $\mathcal{K}^{\text{slope}}_{\text{GEOM}}$ and $\mathcal{K}^{\downarrow\alpha_0}_{\text{GEOM}}$ suggests that the effect of introducing the bathymetry-dependent factor on the domain-wide energy level is analogous to that of reducing the constant GEOMETIRC prefactor α_0. For the experiment with the gentlest sloping bottom (i.e., $1.5W_s$), the diagnosed eddy energy increases by a factor of ~2 compared with the reference experiment, but this increment is not adequately captured by any GEOMETRIC variant. The reason for this underestimation is unclear to the authors but may relate to the simplicity of the eddy energy budget.

When the GEOMETRIC variants $\mathcal{K}_{\text{GEOM}}$ and $\mathcal{K}^{\downarrow\tau_E}_{\text{GEOM}}$ are adopted, the prognostic eddy energy is consistently underestimated, but the variation of the bulk energy magnitude is still qualitatively correct. For instance, $\{E\}$ is clearly predicted to increase with amplified wind or thermal expansion coefficient. Note also that the energy levels predicted with $\mathcal{K}_{\text{GEOM}}$ and $\mathcal{K}^{\downarrow\tau_E}_{\text{GEOM}}$ are nearly identical in each experiment, despite the fact that the eddy energy dissipation time scale in the energy budget differs by a factor of two between these two cases.

To explain the characteristics of domain-wide prognostic eddy energy shown in Fig. 8, one may attempt to analyze the leading-order balance of the eddy energy budget (8) embedded in the GEOMETRIC parameterization. However, the source and dissipation terms that dominate the energy budget are both linearly proportional to the eddy energy. In this case, the eddy energy itself cancels out so that the linear dissipation governs the mean flow baroclinicity [see Eq. (6) of Marshall et al. (2017) and appendix B of Mak et al. (2017)].

A more informative approach is to analyze the momentum balance in a zonally symmetric system, where the momentum injected by surface winds must be transferred downward to the seafloor, primarily through the eddy interfacial form stress $-f_0(\mathcal{F}^y_b/N^2)$ (e.g., Marshall and Speer 2012; Vallis 2017). By parameterizing the interfacial form stress using the GEOMETRIC closure and assuming negligible residual flows, Marshall et al. (2017) derived a scaling of the eddy energy level [see their Eq. (3)], i.e.,

$$E_{\text{pred}} \approx \frac{|\tau|N}{\rho_0 f_0 \alpha_{\text{geom}}}, \tag{14}$$

which suggests that the eddy energy enhances with N/f_0 and wind stress but decreases with the GEOMETRIC prefactor.

Despite the fact that diabatic effects do exist in our coarse-resolution simulations (e.g., temperature restoring at the surface), the theoretically predicted energy following Eq. (14) builds a correlation of 0.87 with the prognostic $\{E\}$ in all simulations incorporating GEOMETRIC variants. The scaling Eq. (14) explains the elevated $\{E\}$ observed in experiments with strengthened wind stress or thermal expansion coefficient (in the latter case, the vertical stratification is strengthened relative to the reference case), and in simulations with $\mathcal{K}^{\text{slope}}_{\text{GEOM}}$ and $\mathcal{K}^{\downarrow\alpha_0}_{\text{GEOM}}$ for which the domain-wide GEOMETRIC prefactor is reduced (Fig. 8). The scaling derived by Marshall et al. (2017) also suggests that the dissipation time scale does not directly control the equilibrated eddy energy level in coarse-resolution simulations. Rather, the dissipation time scale affects the eddy energy level through its impacts on the stratification N/f_0 (e.g., Figs. 3c,e). However, this impact is quantitatively trivial as $\{N/f\}$ increases only by around 2% when τ_E is varied from 40 to 80 days in our simulations.

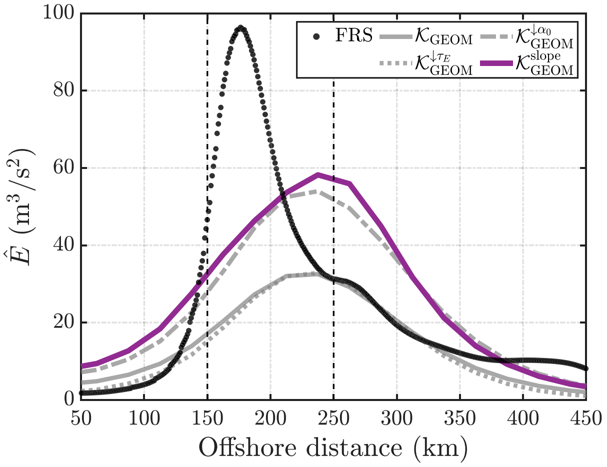

FIG. 9. Depth-integrated total eddy energy diagnosed in the fine-resolution simulation (black dots) and predicted by the energy budget (8) in coarse-resolution simulations (curves) as functions of offshore distance in the reference experiment.

b. Local errors of prognostic eddy energy

Though it is encouraging to find the agreement between the domain-wide prognostic and diagnosed eddy energy for simulations incorporating $\mathcal{K}^{\text{slope}}_{\text{GEOM}}$ and $\mathcal{K}^{\downarrow\alpha_0}_{\text{GEOM}}$ in most experiments (Fig. 8), cautions must be taken because local errors of eddy energy might be substantial in coarse-resolution simulations.

In Fig. 9, we compare the cross-slope variations of the depth-integrated eddy energy predicted by the energy budget (8) in the 25-km run (colored curves) and diagnosed from the 1-km run (black dots) in the equilibrated reference experiment. Local mismatches of eddy energy emerge for all GEOMETRIC variants. For instance, eddy energy in the 25-km simulation incorporating $\mathcal{K}^{\text{slope}}_{\text{GEOM}}$ peaks at 58.2 m^3 s^{-2} at y = 238 km, which contrasts with the energy maximum of 96.4 m^3 s^{-2} at y = 176 km in the fine-resolution simulation. Without including $\mathcal{F}_{\text{GEOM}}$ but using a reduced α_0 in the GEOMETRIC prefactor, $\mathcal{K}^{\downarrow\alpha_0}_{\text{GEOM}}$ produces a nearly identical distribution of prognostic eddy energy as $\mathcal{K}^{\text{slope}}_{\text{GEOM}}$. The other two GEOMETRIC variants $\mathcal{K}_{\text{GEOM}}$ and $\mathcal{K}^{\downarrow\tau_E}_{\text{GEOM}}$ lead to substantially underestimated eddy energy across the latitudinal range of $y \in$ [120, 240 km], due to the overestimated GEOMETRIC prefactor [see Eq. (14)].

To quantify the mismatch between the diagnosed and predicted eddy energy, we define a bulk relative error of eddy energy as

$$\mathcal{E}_E = \frac{\{|\hat{E}_{\text{CR}} - \hat{E}_{\text{FR}}|\}_{\text{Mer}}}{\{\hat{E}_{\text{FR}}\}_{\text{Mer}}}, \tag{15}$$

TABLE 3. The bulk relative error of eddy energy $\mathcal{E}_E$ (%) defined by Eq. (15) produced in coarse-resolution simulations incorporating GEOMETRIC parameterizations $\mathcal{K}_{\text{GEOM}}$, $\mathcal{K}^{\downarrow\alpha_0}_{\text{GEOM}}$, $\mathcal{K}^{\downarrow\tau_E}_{\text{GEOM}}$, and $\mathcal{K}^{\text{slope}}_{\text{GEOM}}$ in all perturbation experiments.

	$\mathcal{K}_{\text{GEOM}}$	$\mathcal{K}^{\downarrow\alpha_0}_{\text{GEOM}}$	$\mathcal{K}^{\downarrow\tau_E}_{\text{GEOM}}$	$\mathcal{K}^{\text{slope}}_{\text{GEOM}}$
$0.5W_s$	42.6	45.6	47.8	48.2
$0.66W_s$	61.6	83.5	60.6	84.2
Ref.	44.4	50.6	44.5	55.8
$1.5W_s$	71.0	52.4	72.9	47.4
$1.5\tau_0$	42.1	38.3	42.4	46.5
$2.0\tau_0$	50.2	32.3	50.6	38.8
$0.5\alpha_\theta$	54.0	57.1	52.5	54.3
$2.0\alpha_\theta$	54.3	48.2	57.6	52.2

where $\{\bullet\}_{\text{Mer}}$ indicates the meridional average operator across the coarse-resolution model domain out of the sponge layer (i.e., $y \in [0, 450]$ km). As listed in Table 3, nonnegligible $\mathcal{E}_E$ are found in all simulations despite the well-constrained domain-wide eddy energy $\{E\}$ by $\mathcal{K}^{\downarrow\alpha_0}_{\text{GEOM}}$ and $\mathcal{K}^{\text{slope}}_{\text{GEOM}}$ (Fig. 8). The averaged values of $\mathcal{E}_E$ across all perturbation experiments are 52.5%, 51.0%, 53.6%, and 53.4% for 25-km simulations incorporating $\mathcal{K}_{\text{GEOM}}$, $\mathcal{K}^{\downarrow\alpha_0}_{\text{GEOM}}$, $\mathcal{K}^{\downarrow\tau_E}_{\text{GEOM}}$, and $\mathcal{K}^{\text{slope}}_{\text{GEOM}}$, respectively. Therefore, incorporating the slope-aware GEOMETRIC variant $\mathcal{K}^{\text{slope}}_{\text{GEOM}}$ does not improve the predicted cross-slope eddy energy distribution.

The substantial local energy errors, however, do not significantly compromise the skill of the slope-aware GEOMETRIC variant $\mathcal{K}^{\text{slope}}_{\text{GEOM}}$ in reconstructing the stratification in coarse-resolution simulations (Fig. 6). This is partly because the errors can at most create a factor of 2–3 difference in eddy energy, but there is a three-orders-of-magnitude variation in the eddy diffusivity across the continental slope and the open ocean (e.g., black dots in Fig. 7). Moreover, the order-of-magnitude variation of eddy buoyancy diffusivity is primarily governed by the variation of the Eady (1949) growth rate. Indeed, $(\int_{-|H|}^{0}\sigma_E\,dz)^{-1}$ in the reference fine-resolution simulation increases from ~30 s m^{-1} at the midslope position (i.e., $y = 200$ km) to ~4600 s m^{-1} at $y = 360$ km (not shown), whereas $\hat{E}$ varies only by a factor of ~6. Therefore, the local errors in the prognostic eddy energy play a secondary role in shaping the spatial structure of the predicted eddy buoyancy diffusivity.

c. *Significance of the variation in domain-wide eddy energy*

The insensitivity of the reconstructed flow baroclinicity to the eddy energy local errors in the GEOMETRIC scheme raises the question of whether the predicted trend of eddy energy in response to external forcing is essential to maintain the predictive skill of GEOMETRIC parameterization across prograde fronts. To address this question, we conducted additional simulations incorporating the slope-aware GEOMETRIC variant but with fixed depth-integrated eddy energy, i.e.,

$$\mathcal{K}^{\text{slope}}_{\text{GEOM}}\big|_{\hat{E}_0} = \alpha_0\mathcal{F}_{\text{GEOM}}\frac{\hat{E}_0}{\displaystyle\int_{-|H|}^{0}\sigma_E\,dz}, \tag{16}$$

in all perturbation experiments, where $\hat{E}_0 = 45\,\text{m}^3\,\text{s}^{-2}$ is a constant depth-integrated eddy energy that allows the reference experiment to achieve matched U_{bc} between the 25- and 1-km simulations. Figure 10 shows the domain-averaged baroclinic velocity U_{bc} in the 25-km runs using GEOMETRIC variants $\mathcal{K}^{\text{slope}}_{\text{GEOM}}$ and $\mathcal{K}^{\text{slope}}_{\text{GEOM}}|_{\hat{E}_0}$ against those in the 1-km runs in all experiments. With fixed eddy energy, the slope-aware GEOMETRIC variant $\mathcal{K}^{\text{slope}}_{\text{GEOM}}|_{\hat{E}_0}$ (yellow bars) significantly overestimates the sensitivity of U_{bc} to amplified wind or thermal expansion coefficient. Specifically, $\mathcal{K}^{\text{slope}}_{\text{GEOM}}|_{\hat{E}_0}$ produces $U_{\text{bc}} = 0.171$ m s^{-1} in the $2\tau_0$ experiment, which exceeds U_{bc} in the fine-resolution simulation by a factor of 2.5. On the contrary, with predicted eddy energy via Eq. (8), the errors in U_{bc} are significantly reduced (purple bars). The bulk variation of eddy energy in simulations with the GEOMETRIC parameterization thus plays a prominent role in predicting the domain-wide eddy restratification.

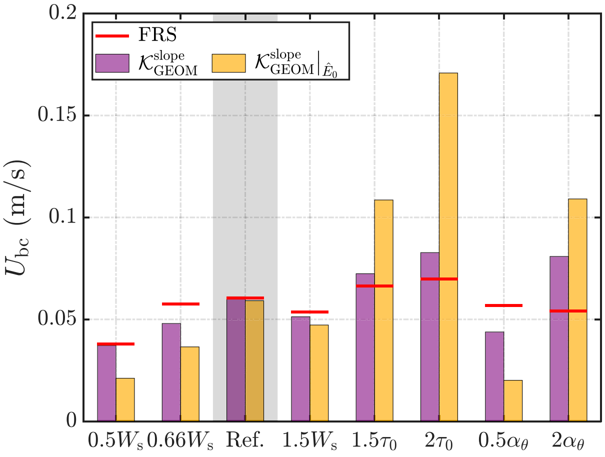

FIG. 10. The domain-averaged baroclinic velocity U_{bc} defined by Eq. (9) in fine-resolution simulations (red lines) against those in coarse-resolution simulations employing GEOMETRIC parameterizations $\mathcal{K}^{\text{slope}}_{\text{GEOM}}$ (purple bars) and $\mathcal{K}^{\text{slope}}_{\text{GEOM}}|_{\hat{E}_0}$ (yellow bars) across all perturbation experiments (see labels on the abscissa and Table 2).

To summarize, the eddy energy budget (8) in the GEOMETRIC parameterization correctly captures the bulk variation of eddy energy across our simulations (Fig. 8), although local errors are present (Fig. 9). These local errors do not compromise the performance of the GEOMETRIC variants, since the order-of-magnitude cross-slope variation of the eddy diffusivity is primarily governed by the Eady (1949) growth rate. Despite the relatively minor role played by the spatial distribution of eddy energy, accurately predicted bulk variations of the eddy energy in response to the environmental changes are crucial for accurately predicting the domain-wide mean flow baroclinicity across the perturbation experiments (Fig. 10).

6. Summary and discussion

In this work, we assess the predictive skill of various GM-based eddy parameterization schemes (Gent and McWilliams

1990; Visbeck et al. 1997; Marshall et al. 2012; Wei et al. 2022) across prograde frontal currents using a set of coarse-resolution simulations, the solutions of which are compared against fine-resolution simulations with otherwise nearly identical model configurations. The main conclusions of this work are as follows:

1) The energetically constrained GEOMETRIC parameterization schemes [i.e., Eqs. (5) and (6)] more accurately predict the domain-wide mean flow baroclinicity in coarse-resolution simulations than constant eddy diffusivities [i.e., Eq. (3)] and the Visbeck et al. (1997) scheme [i.e., Eq. (4)]. This highlights the benefits of coupling a subgrid-scale eddy energy budget with a GM-based scheme in constraining the effects of eddy buoyancy fluxes in coarse-resolution simulations (Mak et al. 2018; Jansen et al. 2019).
2) The slope-aware modification (6b) added into the GEOMETRIC prefactor is crucial for accurately predicting the mean state of prograde currents in coarse-resolution simulations. It leads to a reduction in the predicted eddy diffusivity magnitude over the sloping seafloor while minimally altering the diffusivity magnitude in the relatively flat-bottomed open ocean. The thus formulated slope-aware GEOMETRIC parameterization for eddy buoyancy fluxes outperforms other GM-based parameterization schemes in our coarse-resolution simulations.
3) The eddy energy budget (8) associated with the GEOMETRIC parameterization effectively captures the varying trend of the domain-wide eddy energy level across our perturbation experiments. Despite the local errors in the predicted eddy energy, the prograde mean current state reconstruction in coarse-resolution simulations appears insensitive to these errors. This implies that existing subgrid-scale eddy energy budgets (Mak et al. 2018, 2022b; Jansen et al. 2019; Kong and Jansen 2021) developed for open-ocean environments can maintain their utilities in augmenting eddy parameterizations across steep continental slopes.

Further refinement of the subgrid-scale eddy energy budget entails a better understanding of the eddy energy dissipation rate. Mak et al. (2022a) showed that one could approximate a spatially varying dissipation rate via kinematic-type inference calculation using diagnostics in fine-resolution simulations, and the thus approximated dissipation rate can be further utilized in prognostic simulations. While a spatially varying energy dissipation rate has the potential to improve the prognostic eddy energy budget, the approximation of the dissipation rate via the inference calculation depends on the tunable parameters in the eddy energy budget (e.g., the energy diffusivity and the prefactor of GEOMETRIC variants) as well as parameters in the inference calculation.

This study specifically focuses on prograde flows, which constitute only half of the large-scale shelf/slope flow systems found in nature (e.g., Isachsen 2011). In contrast, retrograde flows are characterized by isopycnals tilted in the same direction as the ocean bottom. Using idealized eddy-resolving simulations, Wang and Stewart (2020) have proposed several energetically constrained slope-aware scalings of eddy buoyancy fluxes across retrograde flows (see their Table 3), which differ in both the relevant parameter dependence (the ratio between topographic slope and depth-averaged isopycnal slope, rather than the slope Burger number, was used in their scaling prefactors) and functional forms from the scheme evaluated in this study. Assessment of the scalings of Wang and Stewart (2020) in coarse-grid simulations of retrograde flows aided by a subgrid-scale eddy energy budget (similar to the one used here) is warranted and ongoing.

There exist other approaches to adapting existing GM-based parameterizations toward continental shelf and slope regions. For instance, a “depth-tapering” scheme has now been implemented in Nucleus for European Modeling of the Ocean model (NEMO) to suppress the GEOMETRIC-based eddy buoyancy diffusivity across shoaling bathymetry. This depth-tapering scheme was devised to rectify the potential over-restratification by the slope-independent GEOMETRIC scheme in shallow regions. It would be of interest to compare the efficacy of the slope-aware modification (6b), which is mainly controlled by the *bottom steepness*, against the depth-tapering scheme in constraining the mean state of the ocean circulation over the continental shelf and slope in a coarse-resolution global simulation.

Recent works on eddy parameterization development highlight the significance of energy backscatter in compensating for the overly large forward energy transfer induced by viscous closures (Juricke et al. 2019, 2020a,b) and in building “resolution awareness” into eddy parameterization schemes for eddy-permitting ocean models (Zanna et al. 2017; Bachman 2019; Jansen et al. 2019). In parallel, Mak et al. (2023) proposed an alternative “splitting” approach to realizing resolution-awareness of GM-based parameterization schemes; these modified schemes mainly shape the large-scale part, defined via the splitting approach, of ocean stratification and allow explicitly resolved mesoscale variability to exist (see their Fig. 3). By contrast, this study has focused solely on the “noneddying” regime. In reality, mesoscale eddies can be partially resolved across the continental slope regions that are close to the open ocean. In such cases, a resolution-aware eddy parameterization scheme may be favored. It is worth investigating whether an energy backscatter scheme or the splitting approach can augment our proposed slope-aware closure if an eddy-permitting grid resolution is employed to resolve part of the mesoscale.

The bathymetry used in this study is symmetric alongshore, which contrasts with the realistic seafloor characterized by a broad spectrum of topographic variations [e.g., see Fig. 12 of de La Lama et al. (2016)]. To maintain the skill of the slope-aware GEOMETRIC parameterization, caution must be taken in calculating the bottom steepness, which dominates the magnitude of the slope Burger number (and thus the slope-awareness modification). Specifically, the slope Burger number following Eq. (7) should reflect the large-scale part of topographic variations (e.g., with spatial scale exceeding the local internal deformation radius; Isachsen 2011), which modulates the background PV gradient (Vallis and Maltrud 1993). Small-scale seafloor roughness, by contrast, is anticipated to mainly modulate the geostrophic turbulence by dissipating the mesoscale eddy energy (Nikurashin et al. 2013; Klymak et al. 2021; Yang et al. 2021; Ruan 2022), and shaping the vertical structure of mesoscale turbulence (Treguier and Hua 1988). These two effects from small-scale seafloor roughness should be incorporated into the dissipation time scale τ_E or by imposing a vertical structure of the parameterized eddy energy in the GEOMETRIC scheme, both of which warrant in-depth investigations. In practice, a coarse-grid (~1/4°) simulation may smooth out most of the fine-scale seafloor structures, and calculating the slope Burger number using the gridscale bathymetric gradient may suffice. However, rigorous quantification of the topographic spectra in ocean models can be necessary. In the presence of seafloor roughness, a spatial filter with a cutoff length scale of the local deformation radius is expected to facilitate the formulation of a slope-aware eddy parameterization.

Several caveats arise from the idealization of our model configurations. First, this study focused exclusively on flows over along-slope symmetric continental slopes, which prevented the formation of standing meanders capable of stratifying the resolved flow (Kong and Jansen 2021; Bai et al. 2021). Moreover, this study did not account for the influence of sea ice, which can modulate the momentum budget of a prograde slope current (Si et al. 2022) and shape the slope frontal structure through ice melting (Silvano et al. 2018). Tidal flows, which have been shown to modulate the heat transport across the Antarctic Slope Front (Stewart et al. 2018; Si et al. 2022), were also neglected. Last, isopycnal eddy diffusion [associated with the Redi (1982) parameterization scheme] can also impact the mean flow stratification in a more realistic ocean controlled by the nonlinear equation of state (e.g., Holmes et al. 2022). Future works are warranted to understand the joint effects of isopycnal eddy diffusion and cross-slope eddy buoyancy fluxes on the mean state of prograde current systems.

Acknowledgments. The authors thank two anonymous reviewers for their detailed comments that improved this article. This work is supported by the Research Grants Council of Hong Kong under awards General Research Fund 16305321 (Y. W.) and Early Career Scheme 2630020 (J. M.), and the Center for Ocean Research, a joint research center between Qingdao National Laboratory for Marine Science and Technology and Hong Kong University of Science and Technology.

Data availability statement. The MITgcm source code (Version checkpoint68n) is archived at https://zenodo.org/record/7621779. The documentation of MITgcm is available on https://mitgcm.readthedocs.io/en/latest/. The modified version of the GEOMETRIC parameterization used in this study has been published at https://github.com/HuaiyuWEI/GEOMETRIC_Slope. Parameter files for the reference fine-resolution and coarse-resolution simulations are available on https://zenodo.org/record/8200677.

APPENDIX A

Sensitivity of $U_{\rm bc}$ to Tunable Parameters in the GEOMETRIC Parameterization

In Fig. A1, we document the variation of $U_{\rm bc}$ in the 25-km simulations incorporating the GEOMETRIC variants, $\mathcal{K}_{\rm GEOM}$ and $\mathcal{K}_{\rm GEOM}^{\rm slope}$, with different values of α_0 or τ_E in the reference experiment. For both GEOMETRIC variants, $U_{\rm bc}$ decreases as the value of $\alpha_{\rm geom}$ or τ_E increases, consistent with the scaling derived in Marshall et al. (2017) [see their Eq. (7)]. Moreover, $U_{\rm bc}$ in simulations incorporating $\mathcal{K}_{\rm GEOM}^{\rm slope}$ is always larger than that in simulations adopting $\mathcal{K}_{\rm GEOM}$ with a fixed set of α_0 and τ_E. This is because the slope-aware modification in $\mathcal{K}_{\rm GEOM}^{\rm slope}$ following (6b) further reduces the GEOMETRIC prefactor $\alpha_{\rm geom}$ over the continental slope (i.e., $\alpha_{\rm geom} \le \alpha_0$).

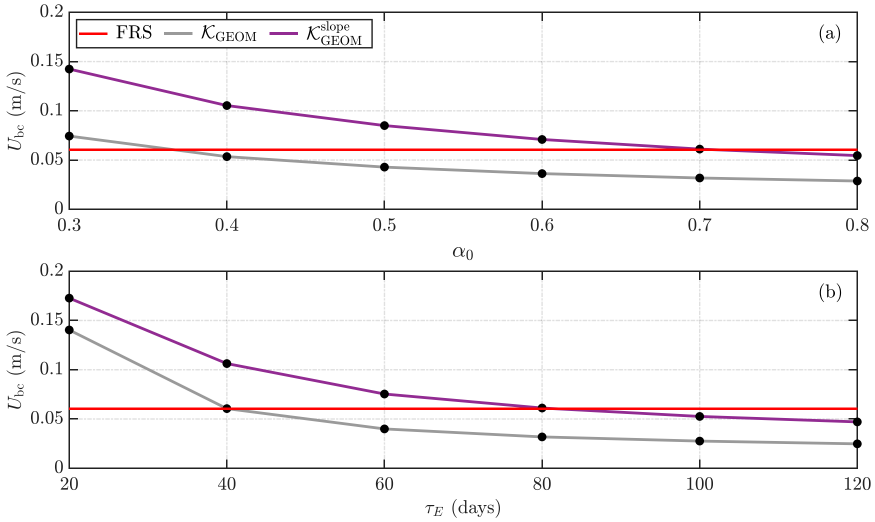

FIG. A1. The domain-averaged baroclinic velocity $U_{\rm bc}$ defined by Eq. (9) in the reference coarse-resolution simulations incorporating $\mathcal{K}_{\rm GEOM}$ (gray line) and $\mathcal{K}_{\rm GEOM}^{\rm slope}$ (purple line) as functions of (a) α_0 and (b) τ_E. In both panels, the red lines indicate $U_{\rm bc}$ in the reference fine-resolution simulation.

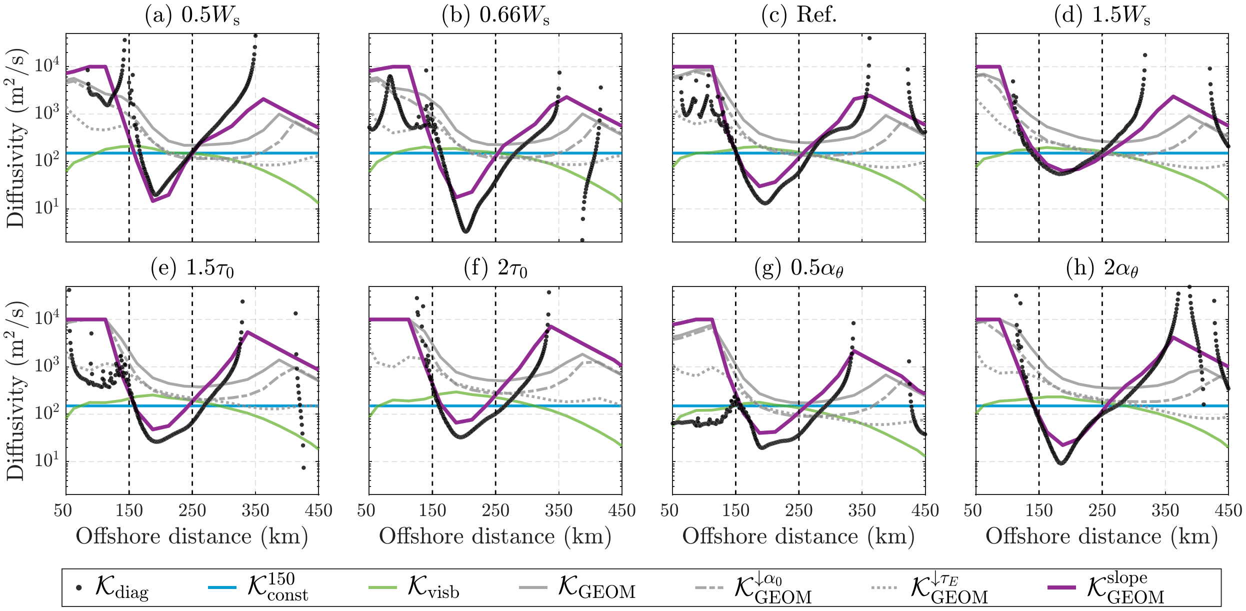

FIG. B1. Eddy buoyancy diffusivity diagnosed in the fine-resolution simulation (black dots) and produced by different GM-based parameterizations in the coarse-resolution simulations (curves) as functions of offshore distance in all perturbation experiments (see panel titles; Table 2).

APPENDIX B

Prognostic Versus Diagnostic Eddy Diffusivities in Perturbation Experiments

Figure B1 shows the diagnosed eddy buoyancy diffusivities following Eq. (13) in 1-km runs (black dots) and the diffusivities predicted by different GM-based parameterizations in 25-km runs (colored curves) in all perturbation experiments (Table 2). The "slope-aware" GEOMETRIC variant $\mathcal{K}^{\text{slope}}_{\text{GEOM}}$ more accurately predicts the offshore variation of $\mathcal{K}_{\text{diag}}$ compared to other variants in all perturbation experiments.

APPENDIX C

Total Eddy Energy in Fine-Resolution Simulations

The calculation of the total eddy energy in fine-resolution simulations exactly follows from Wang and Stewart (2020) and Wei et al. (2022). Specifically, the total eddy energy is formulated as

$$E = \left\langle \frac{1}{|H|}\int_{-|H|}^{0} \text{EKE}\,dz + \frac{1}{|H|}\sum_{i=1}^{N_{\text{lay}}-1} \text{EPE}_i \right\rangle, \tag{C1a}$$

$$\text{EKE} = \frac{1}{2}(\overline{u'^2} + \overline{v'^2}), \tag{C1b}$$

$$\text{EPE}_i = \frac{1}{2}g'_i\overline{\eta'^2_{i+1/2}}, \tag{C1c}$$

where EKE and EPE are respectively the eddy kinetic and potential energies per unit mass, the subscript i stands for the number of isopycnal layers counted from surface to bottom with its maximum indicated by N_{lay}, $g'_i = g(\rho_{i+1} - \rho_i)/\rho_0$ denotes the associated reduced gravity, and $\eta_{i+1/2}$ represents the height of the isopycnal interface between layers i and $i + 1$.

To accurately calculate the EPE, we have defined a sum of $N_{\text{lay}} = 121$ isopycnal layers and transformed the model diagnostics from geopotential coordinates to isopycnal coordinates following Young (2012). Among the selected isopycnal layers, 71 layers fall into the buoyancy (i.e., potential temperature) range of [0°, 10°C] , with their buoyancy intervals chosen based on the prescribed vertical discretization of the buoyancy field in the northern sponge layer, and the remaining 50 layers correspond to the buoyancy range of (10°, 15°C] , with their buoyancy interval fixed at 0.1°C according to the prescribed linear surface temperature profile.

REFERENCES

Abernathey, R., D. Ferreira, and A. Klocker, 2013: Diagnostics of isopycnal mixing in a circumpolar channel. *Ocean Modell.*, **72**, 1–16, https://doi.org/10.1016/j.ocemod.2013.07.004.

Bachman, S. D., 2019: The GM + E closure: A framework for coupling backscatter with the Gent and McWilliams parameterization. *Ocean Modell.*, **136**, 85–106, https://doi.org/10.1016/j.ocemod.2019.02.006.

——, D. P. Marshall, J. R. Maddison, and J. Mak, 2017: Evaluation of a scalar eddy transport coefficient based on geometric constraints. *Ocean Modell.*, **109**, 44–54, https://doi.org/10.1016/j.ocemod.2016.12.004.

Bai, Y., Y. Wang, and A. L. Stewart, 2021: Does topographic form stress impede prograde ocean currents? *J. Phys. Oceanogr.*, **51**, 2617–2638, https://doi.org/10.1175/JPO-D-20-0189.1.

Bashmachnikov, I. L., R. P. Raj, P. Golubkin, and I. E. Kozlov, 2023: Heat transport by mesoscale eddies in the Norwegian and Greenland seas. *J. Geophys. Res. Oceans*, **128**, e2022JC018987, https://doi.org/10.1029/2022JC018987.

Blumsack, S. L., and P. J. Gierasch, 1972: Mars: The effects of topography on baroclinic instability. *J. Atmos. Sci.*, **29**, 1081–1089, https://doi.org/10.1175/1520-0469(1972)029<1081:MTEOTO>2.0.CO;2.

Brink, K. H., 2012: Baroclinic instability of an idealized tidal mixing front. *J. Mar. Res.*, **70**, 661–688, https://doi.org/10.1357/002224012805262716.

——, 2016: Continental shelf baroclinic instability. Part I: Relaxation from upwelling or downwelling. *J. Phys. Oceanogr.*, **46**, 551–568, https://doi.org/10.1175/JPO-D-15-0047.1.

——, and D. A. Cherian, 2013: Instability of an idealized tidal mixing front: Symmetric instabilities and frictional effects. *J. Mar. Res.*, **71**, 425–450, https://doi.org/10.1357/002224013812587582.

Chanut, J., B. Barnier, W. Large, L. Debreu, T. Penduff, J. M. Molines, and P. Mathiot, 2008: Mesoscale eddies in the Labrador Sea and their contribution to convection and restratification. *J. Phys. Oceanogr.*, **38**, 1617–1643, https://doi.org/10.1175/2008JPO3485.1.

Chelton, D. B., R. A. DeSzoeke, M. G. Schlax, K. El Naggar, and N. Siwertz, 1998: Geographical variability of the first baroclinic Rossby radius of deformation. *J. Phys. Oceanogr.*, **28**, 433–460, https://doi.org/10.1175/1520-0485(1998)028<0433:GVOTFB>2.0.CO;2.

Chen, C., and I. Kamenkovich, 2013: Effects of topography on baroclinic instability. *J. Phys. Oceanogr.*, **43**, 790–804, https://doi.org/10.1175/JPO-D-12-0145.1.

Chen, S.-N., C.-J. Chen, and J. A. Lerczak, 2020: On baroclinic instability over continental shelves: Testing the utility of Eady-type models. *J. Phys. Oceanogr.*, **50**, 3–33, https://doi.org/10.1175/JPO-D-19-0175.1.

Cimoli, L., A. Stegner, and G. Roullet, 2017: Meanders and eddy formation by a buoyant coastal current flowing over a sloping topography. *Ocean Sci.*, **13**, 905–923, https://doi.org/10.5194/os-13-905-2017.

Cox, M., 1987: Isopycnal diffusion in a z-coordinate ocean model. *Ocean Modell.*, **74**, 1–5.

Danabasoglu, G., J. C. McWilliams, and P. R. Gent, 1994: The role of mesoscale tracer transports in the global ocean circulation. *Science*, **264**, 1123–1126, https://doi.org/10.1126/science.264.5162.1123.

de La Lama, M. S., J. H. LaCasce, and H. K. Fuhr, 2016: The vertical structure of ocean eddies. *Dyn. Stat. Climate Syst.*, **1** (1), dzw001, https://doi.org/10.1093/climsys/dzw001.

Dunne, J. P., and Coauthors, 2012: GFDL's ESM2 global coupled climate–carbon Earth system models. Part I: Physical formulation and baseline simulation characteristics. *J. Climate*, **25**, 6646–6665, https://doi.org/10.1175/JCLI-D-11-00560.1.

Eady, E. T., 1949: Long waves and cyclone waves. *Tellus*, **1**, 33–52, https://doi.org/10.3402/tellusa.v1i3.8507.

Farneti, R., and P. R. Gent, 2011: The effects of the eddy-induced advection coefficient in a coarse-resolution coupled climate model. *Ocean Modell.*, **39**, 135–145, https://doi.org/10.1016/j.ocemod.2011.02.005.

——, T. L. Delworth, A. J. Rosati, S. M. Griffies, and F. Zeng, 2010: The role of mesoscale eddies in the rectification of the Southern Ocean response to climate change. *J. Phys. Oceanogr.*, **40**, 1539–1557, https://doi.org/10.1175/2010JPO4353.1.

——, and Coauthors, 2015: An assessment of Antarctic Circumpolar Current and Southern Ocean meridional overturning circulation during 1958–2007 in a suite of interannual CORE-II simulations. *Ocean Modell.*, **93**, 84–120, https://doi.org/10.1016/j.ocemod.2015.07.009.

Fox-Kemper, B., S. Bachman, B. Pearson, and S. Reckinger, 2014: Principles and advances in subgrid modelling for eddy-rich simulations. *CLIVAR Exchanges*, No. 65, International CLIVAR Project Office, Southampton, United Kingdom, 42–46, https://www.clivar.org/sites/default/files/documents/exchanges65_0.pdf.

——, and Coauthors, 2019: Challenges and prospects in ocean circulation models. *Front. Mar. Sci.*, **6**, 65, https://doi.org/10.3389/fmars.2019.00065.

Gent, P. R., and J. C. McWilliams, 1990: Isopycnal mixing in ocean circulation models. *J. Phys. Oceanogr.*, **20**, 150–155, https://doi.org/10.1175/1520-0485(1990)020<0150:IMIOCM>2.0.CO;2.

Gerdes, R., C. Köberle, and J. Willebrand, 1991: The influence of numerical advection schemes on the results of ocean general circulation models. *Climate Dyn.*, **5**, 211–226, https://doi.org/10.1007/BF00210006.

Ghaffari, P., P. E. Isachsen, O. A. Nøst, and J. E. Weber, 2018: The influence of topography on the stability of the Norwegian Atlantic Current off northern Norway. *J. Phys. Oceanogr.*, **48**, 2761–2777, https://doi.org/10.1175/JPO-D-17-0235.1.

Greatbatch, R. J., X. Zhai, J.-D. Kohlmann, and L. Czeschel, 2010: Ocean eddy momentum fluxes at the latitudes of the Gulf Stream and the Kuroshio Extensions as revealed by satellite data. *Ocean Dyn.*, **60**, 617–628, https://doi.org/10.1007/s10236-010-0282-6.

Griffies, S. M., 1998: The Gent–McWilliams skew flux. *J. Phys. Oceanogr.*, **28**, 831–841, https://doi.org/10.1175/1520-0485(1998)028<0831:TGMSF>2.0.CO;2.

——, and Coauthors, 2005: Formulation of an ocean model for global climate simulations. *Ocean Sci.*, **1**, 45–79, https://doi.org/10.5194/os-1-45-2005.

Grooms, I., 2017: Simulations of eddy kinetic energy transport in barotropic turbulence. *Phys. Rev. Fluids*, **2**, 113801, https://doi.org/10.1103/PhysRevFluids.2.113801.

Hallberg, R., 2013: Using a resolution function to regulate parameterizations of oceanic mesoscale eddy effects. *Ocean Modell.*, **72**, 92–103, https://doi.org/10.1016/j.ocemod.2013.08.007.

Hátún, H., C. C. Eriksen, and P. B. Rhines, 2007: Buoyant eddies entering the Labrador Sea observed with gliders and altimetry. *J. Phys. Oceanogr.*, **37**, 2838–2854, https://doi.org/10.1175/2007JPO3567.1.

Hetland, R. D., 2017: Suppression of baroclinic instabilities in buoyancy-driven flow over sloping bathymetry. *J. Phys. Oceanogr.*, **47**, 49–68, https://doi.org/10.1175/JPO-D-15-0240.1.

Hill, C., D. Ferreira, J.-M. Campin, J. Marshall, R. Abernathey, and N. Barrier, 2012: Controlling spurious diapycnal mixing in eddy-resolving height-coordinate ocean models–Insights from virtual deliberate tracer release experiments. *Ocean Modell.*, **45–46**, 14–26, https://doi.org/10.1016/j.ocemod.2011.12.001.

Holmes, R. M., S. Groeskamp, K. D. Stewart, and T. J. McDougall, 2022: Sensitivity of a coarse-resolution global ocean model to a spatially variable neutral diffusivity. *J. Adv. Model. Earth Syst.*, **14**, e2021MS002914, https://doi.org/10.1029/2021MS002914.

Isachsen, P. E., 2011: Baroclinic instability and eddy tracer transport across sloping bottom topography: How well does a modified Eady model do in primitive equation simulations? *Ocean Modell.*, **39**, 183–199, https://doi.org/10.1016/j.ocemod.2010.09.007.

——, 2015: Baroclinic instability and the mesoscale eddy field around the Lofoten Basin. *J. Geophys. Res. Oceans*, **120**, 2884–2903, https://doi.org/10.1002/2014JC010448.

——, J. LaCasce, C. Mauritzen, and S. Häkkinen, 2003: Wind-driven variability of the large-scale recirculating flow in the Nordic Seas and Arctic Ocean. *J. Phys. Oceanogr.*, **33**, 2534–2550, https://doi.org/10.1175/1520-0485(2003)033<2534:WVOTLR>2.0.CO;2.

Jansen, M. F., A. Adcroft, S. Khani, and H. Kong, 2019: Toward an energetically consistent, resolution aware parameterization of ocean mesoscale eddies. *J. Adv. Model. Earth Syst.*, **11**, 2844–2860, https://doi.org/10.1029/2019MS001750.

Juricke, S., S. Danilov, A. Kutsenko, and M. Oliver, 2019: Ocean kinetic energy backscatter parametrizations on unstructured grids: Impact on mesoscale turbulence in a channel. *Ocean Modell.*, **138**, 51–67, https://doi.org/10.1016/j.ocemod.2019.03.009.

——, ——, N. Koldunov, M. Oliver, D. V. Sein, D. Sidorenko, and Q. Wang, 2020a: A kinematic kinetic energy backscatter parametrization: From implementation to global ocean simulations. *J. Adv. Model. Earth Syst.*, **12**, e2020MS002175, https://doi.org/10.1029/2020MS002175.

——, ——, ——, ——, and D. Sidorenko, 2020b: Ocean kinetic energy backscatter parametrization on unstructured grids: Impact on global eddy-permitting simulations. *J. Adv. Model. Earth Syst.*, **12**, e2019MS001855, https://doi.org/10.1029/2019MS001855.

Klocker, A., and D. P. Marshall, 2014: Advection of baroclinic eddies by depth mean flow. *Geophys. Res. Lett.*, **41**, 3517–3521, https://doi.org/10.1002/2014GL060001.

Klymak, J. M., D. Balwada, A. N. Garabato, and R. Abernathey, 2021: Parameterizing nonpropagating form drag over rough bathymetry. *J. Phys. Oceanogr.*, **51**, 1489–1501, https://doi.org/10.1175/JPO-D-20-0112.1.

Kong, H., and M. F. Jansen, 2021: The impact of topography and eddy parameterization on the simulated Southern Ocean circulation response to changes in surface wind stress. *J. Phys. Oceanogr.*, **51**, 825–843, https://doi.org/10.1175/JPO-D-20-0142.1.

LaCasce, J. H., and S. Groeskamp, 2020: Baroclinic modes over rough bathymetry and the surface deformation radius. *J. Phys. Oceanogr.*, **50**, 2835–2847, https://doi.org/10.1175/JPO-D-20-0055.1.

Lee, M.-M., A. J. G. Nurser, A. C. Coward, and B. A. de Cuevas, 2007: Eddy advective and diffusive transports of heat and salt in the Southern Ocean. *J. Phys. Oceanogr.*, **37**, 1376–1393, https://doi.org/10.1175/JPO3057.1.

Maddison, J. R., and D. P. Marshall, 2013: The Eliassen–Palm flux tensor. *J. Fluid Mech.*, **729**, 69–102, https://doi.org/10.1017/jfm.2013.259.

Mak, J., D. P. Marshall, J. R. Maddison, and S. D. Bachman, 2017: Emergent eddy saturation from an energy constrained eddy parameterisation. *Ocean Modell.*, **112**, 125–138, https://doi.org/10.1016/j.ocemod.2017.02.007.

——, J. R. Maddison, D. P. Marshall, and D. R. Munday, 2018: Implementation of a geometrically informed and energetically constrained mesoscale eddy parameterization in an ocean circulation model. *J. Phys. Oceanogr.*, **48**, 2363–2382, https://doi.org/10.1175/JPO-D-18-0017.1.

——, A. Avdis, T. David, H. S. Lee, Y. Na, Y. Wang, and F. E. Yan, 2022a: On constraining the mesoscale eddy energy dissipation time-scale. *J. Adv. Model. Earth Syst.*, **14**, e2022MS003223, https://doi.org/10.1029/2022MS003223.

——, D. P. Marshall, G. Madec, and J. R. Maddison, 2022b: Acute sensitivity of global ocean circulation and heat content to eddy energy dissipation time-scale. *Geophys. Res. Lett.*, **49**, e2021GL097259, https://doi.org/10.1029/2021GL097259.

——, J. R. Maddison, D. P. Marshall, X. Ruan, Y. Wang, and L. Yeow, 2023: Scale-awareness in an eddy energy constrained mesoscale eddy parameterization. arXiv, 2306.08988v2, https://doi.org/10.48550/arXiv.2306.08988.

Manucharyan, G. E., and P. E. Isachsen, 2019: Critical role of continental slopes in halocline and eddy dynamics of the Ekman-driven Beaufort Gyre. *J. Geophys. Res. Oceans*, **124**, 2679–2696, https://doi.org/10.1029/2018JC014624.

Marshall, D. P., J. R. Maddison, and P. S. Berloff, 2012: A framework for parameterizing eddy potential vorticity fluxes. *J. Phys. Oceanogr.*, **42**, 539–557, https://doi.org/10.1175/JPO-D-11-048.1.

——, M. H. P. Ambaum, J. R. Maddison, D. R. Munday, and L. Novak, 2017: Eddy saturation and frictional control of the Antarctic Circumpolar Current. *Geophys. Res. Lett.*, **44**, 286–292, https://doi.org/10.1002/2016GL071702.

Marshall, J., and K. Speer, 2012: Closure of the meridional overturning circulation through Southern Ocean upwelling. *Nat. Geosci.*, **5**, 171–180, https://doi.org/10.1038/ngeo1391.

——, A. Adcroft, C. Hill, L. Perelman, and C. Heisey, 1997: A finite-volume, incompressible Navier Stokes model for studies of the ocean on parallel computers. *J. Geophys. Res.*, **102**, 5753–5766, https://doi.org/10.1029/96JC02775.

Mechoso, C. R., 1980: Baroclinic instability of flows along sloping boundaries. *J. Atmos. Sci.*, **37**, 1393–1399, https://doi.org/10.1175/1520-0469(1980)037<1393:BIOFAS>2.0.CO;2.

Nikurashin, M., G. K. Vallis, and A. Adcroft, 2013: Routes to energy dissipation for geostrophic flows in the Southern Ocean. *Nat. Geosci.*, **6**, 48–51, https://doi.org/10.1038/ngeo1657.

Nøst, O. A., and P. E. Isachsen, 2003: The large-scale time-mean ocean circulation in the Nordic Seas and Arctic Ocean estimated from simplified dynamics. *J. Mar. Res.*, **61**, 175–210, https://doi.org/10.1357/002224003322005069.

Pennel, R., A. Stegner, and K. Béranger, 2012: Shelf impact on buoyant coastal current instabilities. *J. Phys. Oceanogr.*, **42**, 39–61, https://doi.org/10.1175/JPO-D-11-016.1.

Phillips, N. A., 1954: Energy transformations and meridional circulations associated with simple baroclinic waves in a two-level, quasi-geostrophic model. *Tellus*, **6**, 274–286, https://doi.org/10.3402/tellusa.v6i3.8734.

Poulin, F. J., A. Stegner, M. Hernández-Arencibia, A. Marrero-Díaz, and P. Sangrà, 2014: Steep shelf stabilization of the coastal Bransfield Current: Linear stability analysis. *J. Phys. Oceanogr.*, **44**, 714–732, https://doi.org/10.1175/JPO-D-13-0158.1.

Poulsen, M. B., M. Jochum, J. R. Maddison, D. P. Marshall, and R. Nuterman, 2019: A geometric interpretation of Southern Ocean eddy form stress. *J. Phys. Oceanogr.*, **49**, 2553–2570, https://doi.org/10.1175/JPO-D-18-0220.1.

Prather, M. J., 1986: Numerical advection by conservation of second-order moments. *J. Geophys. Res.*, **91**, 6671–6681, https://doi.org/10.1029/JD091iD06p06671.

Redi, M. H., 1982: Oceanic isopycnal mixing by coordinate rotation. *J. Phys. Oceanogr.*, **12**, 1154–1158, https://doi.org/10.1175/1520-0485(1982)012<1154:OIMBCR>2.0.CO;2.

Ruan, X., 2022: Note on the bulk estimate of the energy dissipation rate in the oceanic bottom boundary layer. *Fluids*, **7**, 82, https://doi.org/10.3390/fluids7020082.

Scott, R. B., and B. K. Arbic, 2007: Spectral energy fluxes in geostrophic turbulence: Implications for ocean energetics. *J. Phys. Oceanogr.*, **37**, 673–688, https://doi.org/10.1175/JPO3027.1.

Si, Y., A. L. Stewart, and I. Eisenman, 2022: Coupled ocean–sea ice dynamics of the Antarctic Slope Current driven by topographic eddy suppression and sea ice momentum redistribution. *J. Phys. Oceanogr.*, **52**, 1563–1589, https://doi.org/10.1175/JPO-D-21-0142.1.

——, ——, and ——, 2023: Heat transport across the Antarctic Slope Front controlled by cross-slope salinity gradients. *Sci. Adv.*, **9**, eadd7049, https://doi.org/10.1126/sciadv.add7049.

Silvano, A., S. R. Rintoul, B. Peña-Molino, W. R. Hobbs, E. van Wijk, S. Aoki, T. Tamura, and G. D. Williams, 2018: Freshening by glacial meltwater enhances melting of ice shelves and reduces formation of Antarctic Bottom Water. *Sci. Adv.*, **4**, eaap9467, https://doi.org/10.1126/sciadv.aap9467.

Søiland, H., and T. Rossby, 2013: On the structure of the Lofoten Basin eddy. *J. Geophys. Res. Oceans*, **118**, 4201–4212, https://doi.org/10.1002/jgrc.20301.

Spall, M. A., 2004: Boundary currents and watermass transformation in marginal seas. *J. Phys. Oceanogr.*, **34**, 1197–1213, https://doi.org/10.1175/1520-0485(2004)034<1197:BCAWTI>2.0.CO;2.

——, 2010a: Dynamics of downwelling in an eddy-resolving convective basin. *J. Phys. Oceanogr.*, **40**, 2341–2347, https://doi.org/10.1175/2010JPO4465.1.

——, 2010b: Non-local topographic influences on deep convection: An idealized model for the Nordic Seas. *Ocean Modell.*, **32**, 72–85, https://doi.org/10.1016/j.ocemod.2009.10.009.

Stewart, A. L., and A. F. Thompson, 2013: Connecting Antarctic cross-slope exchange with Southern Ocean overturning. *J. Phys. Oceanogr.*, **43**, 1453–1471, https://doi.org/10.1175/JPO-D-12-0205.1.

——, A. Klocker, and D. Menemenlis, 2018: Circum-Antarctic shoreward heat transport derived from an eddy-and tide-resolving simulation. *Geophys. Res. Lett.*, **45**, 834–845, https://doi.org/10.1002/2017GL075677.

Thompson, A. F., and K. J. Heywood, 2008: Frontal structure and transport in the northwestern Weddell Sea. *Deep-Sea Res. I*, **55**, 1229–1251, https://doi.org/10.1016/j.dsr.2008.06.001.

——, A. L. Stewart, P. Spence, and K. J. Heywood, 2018: The Antarctic Slope Current in a changing climate. *Rev. Geophys.*, **56**, 741–770, https://doi.org/10.1029/2018RG000624.

Todd, A., and Coauthors, 2020: Ocean-only FAFMIP: Understanding regional patterns of ocean heat content and dynamic sea level change. *J. Adv. Model. Earth Syst.*, **12**, e2019MS002027, https://doi.org/10.1029/2019MS002027.

Treguier, A. M., and B. L. Hua, 1988: Influence of bottom topography on stratified quasi-geostrophic turbulence in the ocean. *Geophys. Astrophys. Fluid Dyn.*, **43**, 265–305, https://doi.org/10.1080/03091928808208867.

Trodahl, M., and P. E. Isachsen, 2018: Topographic influence on baroclinic instability and the mesoscale eddy field in the northern North Atlantic Ocean and the Nordic Seas. *J. Phys. Oceanogr.*, **48**, 2593–2607, https://doi.org/10.1175/JPO-D-17-0220.1.

Uchida, T., D. Balwada, R. P. Abernathey, G. A. McKinley, S. K. Smith, and M. Lévy, 2020: Vertical eddy iron fluxes support primary production in the open Southern Ocean. *Nat. Commun.*, **11**, 1125, https://doi.org/10.1038/s41467-020-14955-0.

Vallis, G. K., 2017: *Atmospheric and Oceanic Fluid Dynamics*. Cambridge University Press, 946 pp.

——, and M. E. Maltrud, 1993: Generation of mean flows and jets on a beta plane and over topography. *J. Phys. Oceanogr.*, **23**, 1346–1362, https://doi.org/10.1175/1520-0485(1993)023<1346:GOMFAJ>2.0.CO;2.

Visbeck, M., J. Marshall, T. Haine, and M. Spall, 1997: Specification of eddy transfer coefficients in coarse-resolution ocean circulation models. *J. Phys. Oceanogr.*, **27**, 381–402, https://doi.org/10.1175/1520-0485(1997)027<0381:SOETCI>2.0.CO;2.

Wang, Y., and A. L. Stewart, 2020: Scalings for eddy buoyancy transfer across continental slopes under retrograde winds. *Ocean Modell.*, **147**, 101579, https://doi.org/10.1016/j.ocemod.2020.101579.

Wei, H., Y. Wang, A. L. Stewart, and J. Mak, 2022: Scalings for eddy buoyancy fluxes across prograde shelf/slope fronts. *J. Adv. Model. Earth Syst.*, **14**, e2022MS003229, https://doi.org/10.1029/2022MS003229.

Yang, Z., X. Zhai, D. P. Marshall, and G. Wang, 2021: An idealized model study of eddy energetics in the western boundary "graveyard." *J. Phys. Oceanogr.*, **51**, 1265–1282, https://doi.org/10.1175/JPO-D-19-0301.1.

Yankovsky, E., L. Zanna, and K. S. Smith, 2022: Influences of mesoscale ocean eddies on flow vertical structure in a resolution-based model hierarchy. *J. Adv. Model. Earth Syst.*, **14**, e2022MS003203, https://doi.org/10.1029/2022MS003203.

Young, W. R., 2012: An exact thickness-weighted average formulation of the Boussinesq equations. *J. Phys. Oceanogr.*, **42**, 692–707, https://doi.org/10.1175/JPO-D-11-0102.1.

Zanna, L., P. P. Mana, J. Anstey, T. David, and T. Bolton, 2017: Scale-aware deterministic and stochastic parametrizations of eddy-mean flow interaction. *Ocean Modell.*, **111**, 66–80, https://doi.org/10.1016/j.ocemod.2017.01.004.

Zhao, J., A. Bower, J. Yang, X. Lin, and N. P. Holliday, 2018: Meridional heat transport variability induced by mesoscale processes in the subpolar North Atlantic. *Nat. Commun.*, **9**, 1124, https://doi.org/10.1038/s41467-018-03134-x.